

**Engineered bio-heterojunction confers extra- and intracellular bacterial ferroptosis and hunger-triggered cell protection for diabetic wound repair**

*Wenyu Dai, Rui Shu, Fan Yang, Bin Li, Hannah M. Johnson, Sheng Yu, Hang Yang, Yau Kei Chan, Weizhong Yang\*, Ding Bai\*, Yi Deng\**

W. Dai, R. Shu, F. Yang, B. Li, W. Yang, D. Bai, Y. Deng

West China School of Stomatology, College of Biomedical Engineering, School of Chemical Engineering, Sichuan University, Chengdu 610041, China.

E-mail: ywz@scu.edu.cn; baiding@scu.edu.cn; dengyibandeng@scu.edu.cn.

W. Dai, R. Shu, F. Yang, B. Li, D. Bai

State Key Laboratory of Oral Diseases, National Clinical Research Center for Oral Diseases, Department of Orthodontics and Pediatric Dentistry, West China Hospital of Stomatology, Sichuan University Chengdu 610065, P. R. China

H. M. Johnson, S. Yu

Department of Chemistry, Washington State University, Pullman, WA 99164, USA

H. Yang

College of Biomedical Engineering, Sichuan University, Chengdu 610065, China.

This article has been accepted for publication and undergone full peer review but has not been through the copyediting, typesetting, pagination and proofreading process, which may lead to differences between this version and the [Version of Record](#). Please cite this article as [doi: 10.1002/adma.202305277](https://doi.org/10.1002/adma.202305277).

This article is protected by copyright. All rights reserved.

Y. K. Chan

Department of Ophthalmology, The University of Hong Kong, Hong Kong 999077, China

Y. Deng

State Key Laboratory of Polymer Materials Engineering, Sichuan University, Chengdu 610065, China.

Y. Deng

Department of Mechanical Engineering, The University of Hong Kong, Hong Kong 999077, China.

**Keywords:** bio-heterojunction, antibacterial, ferroptosis, cell protection, cutaneous regeneration

### Abstract

Nanomaterial-mediated ferroptosis has garnered considerable interest in the antibacterial field, as it invokes the disequilibrium of ion homeostasis and boosts lipid peroxidation in extra- and intracellular bacteria. However, current ferroptosis-associated antibacterial strategies indiscriminately pose damage to healthy cells, ultimately compromising their biocompatibility. To address this daunting issue, we have designed a precise ferroptosis bio-heterojunction (F-bio-HJ) consisting of  $\text{Fe}_2\text{O}_3$ ,  $\text{Ti}_3\text{C}_2$ -MXene, and glucose oxidase (GOx) to induce extra-intracellular bacteria-targeted ferroptosis for infected diabetic cutaneous regeneration.  $\text{Fe}_2\text{O}_3/\text{Ti}_3\text{C}_2$ -MXene@GOx (FMG) catalytically generates a considerable amount of ROS which assaults the membrane of extracellular bacteria, facilitating the permeation of synchronously generated  $\text{Fe}^{2+}/\text{Fe}^{3+}$  into bacteria under near-infrared (NIR) irradiation, causing planktonic bacterial death *via* ferroptosis,  $\text{Fe}^{2+}$  overload, and lipid peroxidation. Additionally, FMG facilitates intracellular bacterial ferroptosis by transporting  $\text{Fe}^{2+}$  into intracellular bacteria *via* inward ferroportin (FPN). With GOx consuming glucose, FMG creates hunger protection which helps macrophages escape cell ferroptosis by activating the adenosine 5'-monophosphate (AMP)-activated protein kinase (AMPK) pathway. *In vivo* results authenticate that

This article is protected by copyright. All rights reserved.

FMG boosts diabetic infectious cutaneous regeneration without triggering ferroptosis in normal cells. As envisaged, the proposed tactic provides a promising approach to combat intractable infections by precisely terminating extra-intracellular infection *via* steerable ferroptosis, thereby markedly elevating the biocompatibility of therapeutic ferroptosis-mediated strategies.

## 1. Introduction

Bacterial infection is recognized as one of the most prominent threats to public health due to limited treatment strategies and severe physical consequences, including amputation and death.<sup>[1–4]</sup> The invasion of the blood circulatory system by bacteria leads to not only severe extracellular infections but also intracellular infections, as certain pathogens can become endocytosed following adhesion to host cells within minutes of exposure.<sup>[5]</sup> Once endocytosed, the surviving intracellular bacteria can then multiply up to tenfold within 24 h while evading the host's immunological response and subverting immune cells from within, ultimately suppressing immune function<sup>[6]</sup> and increasing the difficulty of extracellular sterilization. Further, imperfect clearance of bacteria from within bloodborne phagocytes may enable these invaded cells to act as 'Trojan horses' for later dissemination of the pathogens to local tissues after cell death.<sup>[7–9]</sup> Although potent antibiotics such as penicillin and gentamicin are widely used in traditional treatments, they gradually provide diminishing management of extra-intracellular bacterial infections, brought on by various factors such as the antibiotics' lower permeability through cytomembrane and abated intracellular antibacterial activity, which eventually leads to clinical failure.<sup>[10–14]</sup> Therefore, novel strategies that enact effective sterilization with both extracellular and intracellular antibacterial potency are highly desired.

Ferroptosis, an iron-associated programmed cell death form, is emerging as a promising approach for extracellular and intracellular antibacterial therapies since iron is a universal and necessary component of life.<sup>[15–17]</sup> It is generally considered that ferroptosis occurs when reactive oxygen species (ROS), which are generated by intracellular Fenton reactions utilizing  $\text{Fe}^{2+}$ , sufficiently catalyzes the lipid peroxidation of polyunsaturated fatty acids (PUFAs) on the cell membrane.<sup>[18]</sup> Despite the fact that most bacterial membranes are composed primarily of saturated or monounsaturated lipids, certain bacteria have the ability to synthesize PUFAs or obtain them from

external sources and assimilate them into their membranes. These PUFAs are readily oxidizable, making them substrates to generate proferroptotic signals. As iron metabolism also occurs in bacteria, increasing both the uptake of unstable iron ions in bacteria and the degree of lipid peroxidation through  $\text{Fe}^{2+}$  and ROS transport to jointly induce ferroptosis has emerged as a promising approach to eradicate bacteria. Previous studies have successfully demonstrated that iron-based nanomaterials can rapidly exterminate extracellular methicillin-resistant *Staphylococcus aureus* (MRSA), *Staphylococcus aureus* (*S. aureus*), and *Escherichia coli* (*E. coli*) via accelerating lipid peroxidation by catalyzing  $\text{Fe}^{2+}$  and ROS generation with or without near-infrared (NIR) irradiation.<sup>[16,19–22]</sup> Moreover, ferroptosis is also a reliable strategy for assisting intracellular sterilization, as macrophages have an inward ferroportin (FPN) transport system that brings  $\text{Fe}^{2+}$  to the intracellular bacterial compartment, where a high concentration of  $\text{Fe}^{2+}$  induces ferroptosis-like death of uptaken bacteria<sup>[15,23]</sup>. However, it is possible for the innate highly efficient redox system which counteracts uncontrolled lipid peroxidation, which includes selenium-dependent glutathione peroxidase-4 (GPX4) system,<sup>[24]</sup> ferroptosis suppressor protein 1 (FSP1)-coenzyme Q10 (CoQ<sub>10</sub>) pathway,<sup>[25]</sup> as well as glutamine transport system,<sup>[26,27]</sup> to become overwhelmed by the non-selective ROS and  $\text{Fe}^{2+}$ , leading to unintentional damage towards host cells. Inspired by these findings, we considered that inducing augmented protection of host cells against ferroptosis may be an effective means to improving bactericidal selectivity, ultimately leading to much better biocompatibility of therapeutic ferroptotic technologies.

Unbridled iron-dependent lipid peroxidation is a common downstream cellular event that leads to cellular membrane rupture and ferroptosis. Several innate anti-ferroptosis systems such as system  $x_c^-$  cystine-glutathione (GSH)-GPX4,<sup>[28]</sup> NADPH- FSP1-CoQ<sub>10</sub>,<sup>[29]</sup> GTP cyclohydrolase 1 (GCH1)-tetrahydrobiopterin (BH<sub>4</sub>),<sup>[30]</sup> and dihydroorotate dehydrogenase (DHODH)-CoQ<sub>10</sub><sup>[31]</sup> function to reduce the activity of intracellular Fenton reactions or to remove lipid peroxides (referred to phospholipid hydroperoxides, PLOOHs) generated in phospholipid membranes.<sup>[18]</sup> Thus, inhibiting the progress of lipid peroxidation in cells is the key to protecting cells from ferroptosis. Given that lipids containing PUFAs with labile bis-allylic hydrogen atoms are most susceptible to lipid peroxidation and are necessary for the normal execution of ferroptosis,<sup>[32]</sup> actively suppressing the biosynthesis of these PUFAs is a promising way to add exogenous protection against ferroptosis. Interestingly, it is reported that PUFA-containing lipid biosynthesis can be restrained by adenosine 5'-monophosphate (AMP)-activated protein kinase (AMPK) activation induced by glucose starvation,

thus suppressing ferroptosis.<sup>[33]</sup> As glucose is necessary for ferroptosis, we choose glucose oxidase (GOx) as a hunger protection trigger to consume glucose and induce starvation in normal cells, hence activating the AMPK signal pathway and shielding cells from ferroptosis, consequently accomplishing bacteria-targeted ferroptosis.

Taking the foregoing considerations, an innovative bacteria-targeted F-bio-HJ consisting of  $\text{Fe}_2\text{O}_3/\text{Ti}_3\text{C}_2$ -MXene and GOx was conceived and fabricated in the present work. In this approach,  $\text{Fe}_2\text{O}_3/\text{Ti}_3\text{C}_2$ -MXene@GOx (FMG) bio-HJ possesses the advantages of heterojunctions and demonstrates superb photothermal, photodynamic, and chemodynamic properties<sup>[34]</sup> to catalyze the generation of overwhelming ROS and trigger  $\text{Fe}^{2+}$  iron overload under NIR irradiation. We assumed that  $\text{Fe}_2\text{O}_3$  (FO) leaches more  $\text{Fe}^{3+}$  under acidic conditions, which oxidizes GSH to produce  $\text{Fe}^{2+}$ . The NIR photothermal therapy (PTT) enhances the penetration ability of the bacterial membrane, accelerating the entry of  $\text{Fe}^{2+}$  and ROS into extracellular bacteria and rapidly eliminating them *via* ferroptosis. Another fraction of  $\text{Fe}^{2+}$  was also transported into intracellular bacteria *via* inward FPN transportation in macrophages, triggering further ferroptosis in endocytosed pathogens. Finally, GOx consumes glucose to activate the AMPK signal way for cellular ferroptosis prevention. Both *in vitro* and *in vivo* evaluations were conducted to authenticate the extra-intracellular antibacterial and biological effectiveness anticipated by our design principle. We believe our work presents an entirely new path for the advancement of research into novel ferroptosis-mediated, antibacterial nanomaterials.

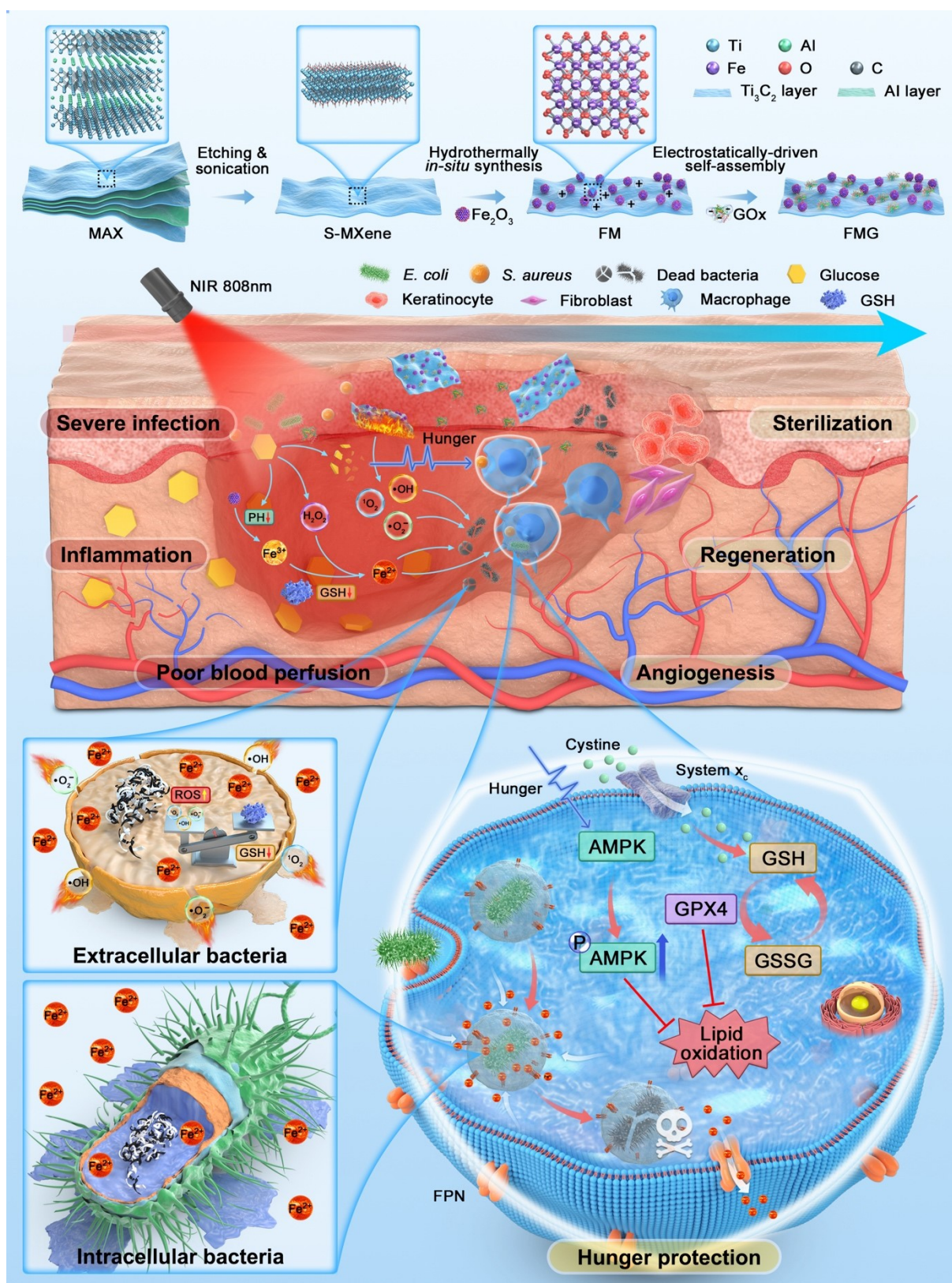
## 2. Results and Discussion

### 2.1. Preparation and characterization of F-bio-HJ

To address the high complication and failure rate of extra-intracellular bacterial infection in diabetic wounds, we originally designed and developed a novel multifunctional F-bio-HJ, FMG, with the ability to induce extra- and intracellular bacteria-targeted ferroptosis, protect normal cells, and facilitate tissue regeneration. As shown in **Figure 1**, to increase the photocatalysis efficiency of  $\text{Ti}_3\text{C}_2$ -MXene, we broaden the surface area by producing ultrathin single-layer  $\text{Ti}_3\text{C}_2$ -MXene (S-MXene) nanosheets through a typical solution-phase exfoliation method followed by ultrasonic delamination as previously reported. To provide sufficient iron for ferroptosis, we choose semiconductive  $\alpha$ - $\text{Fe}_2\text{O}_3$

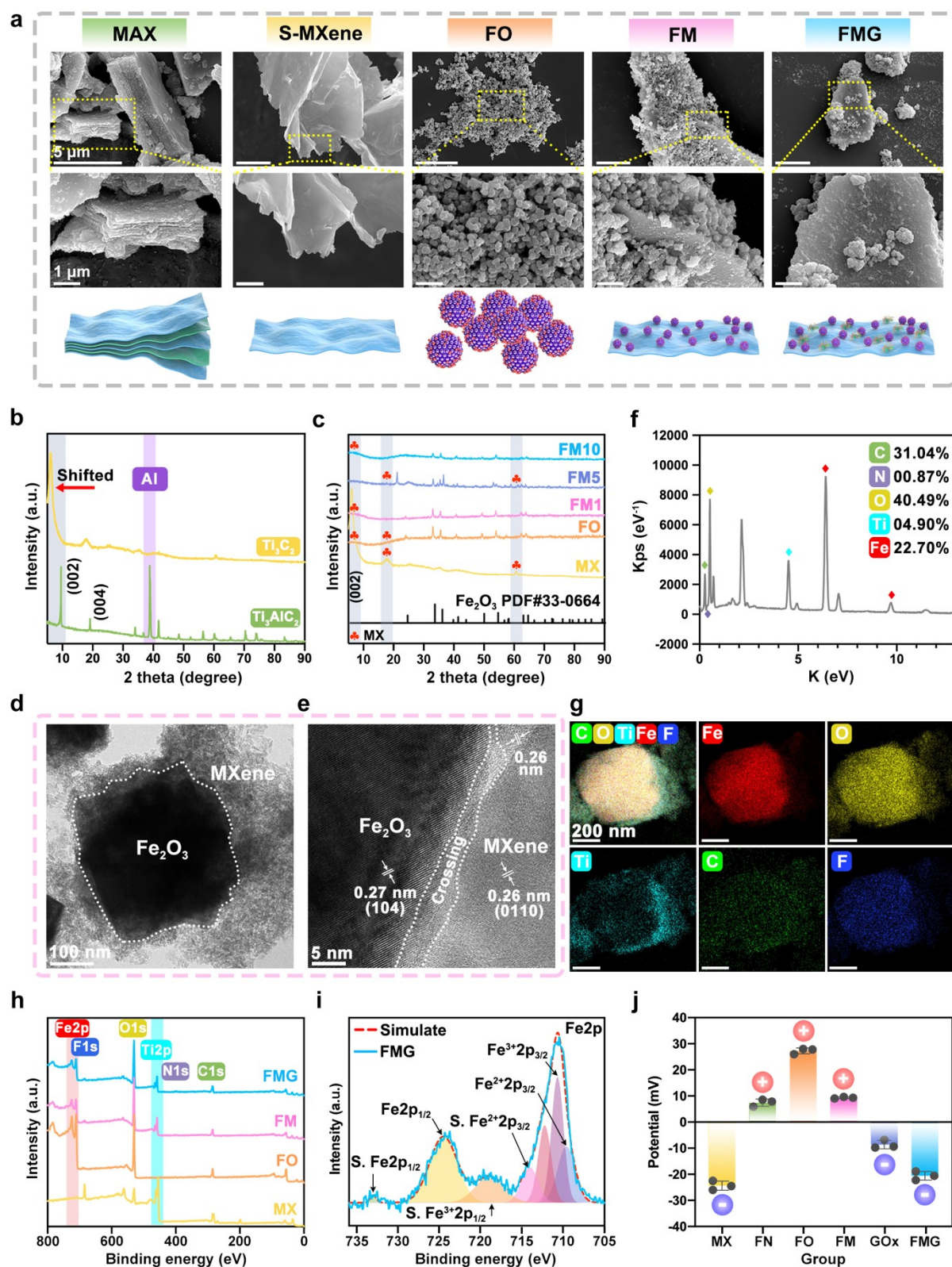
as the iron donor, which is the most common, accessible, and stable iron oxide in nature. The addition of  $\alpha\text{-Fe}_2\text{O}_3$  to MX is done by intercalating it onto MX by the hydrothermal process, resulting in the formation of FM HJ. Finally, to take full advantage of glucose, GOx, which consumes glucose to create a “hunger” signal and catalyzes  $\text{H}_2\text{O}_2$  and acid, is self-assembled onto FM through the electrostatic interaction to form the final F-bio-HJ, FMG.

The morphology and structure of prepared products were first characterized by field emission scanning electron microscopy (FE-SEM). As shown in **Figure 2a**, MAX ( $\text{Ti}_3\text{AlC}_2$ ) has a clear complex structure with a rough surface, while the S-MXene is a smooth two-dimensional film structure accompanied by a few folds.  $\alpha\text{-Fe}_2\text{O}_3$  is spherical small particles at the nanometer level (**Figure S1a**) agglomerated into a block structure at the micron level. After electrostatic adsorption between FO and MX, the smooth MX surface is covered by the agglomerated FO with a smaller size of about 400-600 nm, possibly due to the fact that the negative groups on the surface of MX affect the agglomeration of FO during crystallization. The FMG microscopic morphology is similar to that of FM, which has aggregated FO particles adhered to its lamellar material surface. Moreover, the average particle size of FM and FMG is  $261.33 \pm 4.96$  and  $280.50 \pm 6.75$  nm, respectively (**Figure S1b**).



This article is protected by copyright. All rights reserved.

**Figure 1. Schematic diagram of F-bio-HJs.** Flowchart of the preparation steps and procedure for FMG bio-HJ (F-bio-HJ) and the mechanism of extra-intracellular bacteria-targeted ferroptosis and hunger-triggered cell protection induced by F-bio-HJ.



This article is protected by copyright. All rights reserved.

**Figure 2. Characterization of FM and FMG bio-HJs.** (a) SEM of MAX, S-MXene, FO, FM, and FMG. XRD of (b)  $Ti_3C_2$ ,  $Ti_3AlC_2$ , and (c) FO, MX, FM1, FM5, and FM10. (d) TEM, and (e) HRTEM of FM. (f) EDS analysis of FMG. (g) Elemental mapping of FM. (h) Total XPS spectrum of MX, FO, FM, and FMG. (i) Fe 2p XPS spectrum of FMG. S. represents the Satellite peak. (j) Zeta potential of MX,  $Fe(NO_3)_3$  (FN), FO, FM, GOx, and FMG.

The crystal structure of the hydrothermal products was then characterized by X-Ray diffraction (XRD). Compared with MAX, the strong peak corresponding to the Al layer disappears in the spectrum of MX. Besides, the (002) peak exhibits a decline in sharpness, accompanied by a shift from  $9.55^\circ$  in MAX to  $6.19^\circ$  in MX, due to the removal of the Al layer in the MAX (**Figure 2b**). As shown in **Figure 2c**, the FO prepared through the solvent thermal method corresponds highly to the  $\alpha-Fe_2O_3$  standard card (PDF#33-0664) without obvious spurious peaks with sharp peak shapes, implying ideal crystallinity and purity. To confirm the optimal mass ratio between FO and MX, we noted FO/MX at a mass ratio of 1:1, 5:1, and 10:1 as FM1, FM5, and FM10. The XRD spectra of FM1 and FM10 are basically consistent with FO, and only a (002) diffraction peak at  $2\theta \approx 5^\circ$  is attributed to MX, indicating that the crystallinity of  $Ti_3C_2$  decreases after the solvent thermal reaction. There are spurious peaks at  $2\theta \approx 20^\circ$  and  $2\theta \approx 38^\circ$  in FM5, which may be part of the unetched Al layer in  $Ti_3C_2$  MX. Combining the above results, FO with high purity and good crystallinity was successfully prepared and successfully loaded on S-MXene.

To further analyze the structure and the elemental distribution, we measured FM and FMG using transmission electron microscopy (TEM), high-resolution TEM (HR-TEM), and energy disperse spectroscopy (EDS). From **Figure 2d**, FO crystals are highly oriented with clear lattice stripes, while MX is disordered in orientation with unclear lattice stripes. HRTEM results confirm that there is a different crystal lattice cross at the interface, pointing to the existence of a heterogeneous interface between FO and MX (**Figure 2e**). The interplanar spacings of FO and MX were determined to be approximately 0.27 nm and 0.26 nm, respectively, which correspond to the crystal plane spacings of FO (104) and MX (010). In addition, the EDS image of FM revealed the presence of Fe, O, Ti, C, and F, nearly uniformly distributed throughout the material, suggesting that FO nanoparticles are evenly combined with MX nanosheets (**Figure 2g**). Furthermore, as showcased in **Figure 2f**, the EDS spectrum demonstrates that FMG mainly contains C, N, O, Ti, and Fe, among which the N element is

from GOx. The quantitative atomic percentage results with O element to Fe element ratios greater than 3:2 and C element to Ti element ratios greater than 2:3 is due to the presence of O element to C element in the GOx, indicating the presence of GOx on the FM surface.

In order to further verify the chemical state of elements in various materials and the successful loading of GOx on the FM surface, X-ray photoelectron spectroscopy (XPS) analysis, Zeta potential analysis, and protein detection of FMG bio-HJs were performed. As shown in **Figure 2h**, the full-scan XPS spectrum of MX contains Ti 2p (459 eV), C 1s (285 eV), O 1s (532 eV), and F 1s (686 eV) peaks without Al peaks, suggesting the successful etching of Al layer from MAX ( $\text{Ti}_3\text{AlC}_2$ ). Meanwhile, only Fe 2p (720 eV) O 1s and C 1s peaks are found in the XPS spectrum of FO. **Figure S2a, c, and e** image the high-resolution Ti 2p, C 1s, and O 1s spectrum of MX and **Figure S2b and g** image the high-resolution O 1s and Fe 2p spectrum of FO. The full-scan XPS spectrum of FM is similar to that of FO with the addition of Ti 2p and F 1s peak, indicating the successful composition of FM. **Figure S2d and h** image the high-resolution Ti 2p and Fe 2p spectrum of FM. In addition, the new N 1s peak (400 eV) appears in the FMG spectrum, implying successful loading of GOx, corresponding to the EDS results. **Figure 2i** and **Figure S2f and i** show the Fe 2p, C 1s and N 1s spectrum for FMG. In the high-resolution Fe 2p spectrum of FM and FMG (**Figure S2h** and **Figure 2i**), the enhancement of  $\text{Fe}^{2+}$  contribution indicates electron transferring, compared to FO (**Figure S2g**). In the C 1s spectrum (**Figure S2f**), the peak corresponding to the C-Ti was not detected, probably because the surface of FMG was covered by GOx and FO or the surface of MX was oxidized to  $\text{TiO}_2$ . Besides, a peak for C-N appears at 286.4 eV in C 1s spectrum and a peak for N-H appears at 399.8 eV in N 1s spectrum (**Figure S2i**), implying that GOx was successfully loaded on the surface of FM. Subsequently, the results displayed in **Figure 2j** imply the  $\text{Fe}^{3+}$ , of which  $\zeta$  potential is  $7.42 \pm 1.38$  mV, is adsorbed on the surface of MX with a  $\zeta$  potential of  $-24.33 \pm 1.76$  mV. FM has the  $\zeta$  potential of  $9.33 \pm 0.28$  mV due to the positive charge of  $27.27 \pm 1.10$  mV of FO. Notably,  $\zeta$  potential of FMG decreases to  $-20.57 \pm 1.65$  mV because GOx ( $-8.65 \pm 1.61$  mV) has an opposite surface charge to FM, ascribed to electrostatic interactions between FM and GOx. More intuitively, the total protein content level of FMG steeply increases to a high level because of the GOx coating with an encapsulation efficiency of 42.63% and a loading capacity of 0.086% (**Figure S3**). Similarly, the Fourier transform infrared (FT-IR) spectrum of prepared MX, FO, FM, FMG and GOx also reveal the stable loading of GOx on FMG (**Figure S4a**) since the observed peaks around 1070, 1401, and 2961  $\text{cm}^{-1}$  signify the presence of C-H benzene, C-N, and  $-\text{CH}_2$  bonds in the FT-IR spectrum of GOx and FMG but not FM.

## 2.2. Photothermal, photodynamic and chemodynamic properties of F-bio-HJ

We first evaluated the photothermal, photodynamic, and chemodynamic performance of the bio-HJs. Initially, we verified the highly favorable thermal response possessed by FMG (Supporting Results 2.1 and **Figure S5**) induced by NIR irradiation. Then photodynamic capability, which is closely related to electron-hole separation and ROS production efficiency,<sup>[35]</sup> was estimated by UV–visible diffuse reflectance spectroscopy (UV–vis DRS). As shown in **Figure S4b**, FO exhibits prominent absorption in the spectrum below 600 nm. However, after forming HJs with different ratios of MX, FM exhibits enhanced absorption in the NIR region. Among FM HJs, the absorbance of FM1 and FM5 in the NIR region are similar, but both are lower than that of FM10, indicating that FM10 will possess more robust photothermal performance. The increased absorbance at 808 nm will also serve to enhance photodynamic response and result in a stronger anti-infective effect in downstream therapeutic applications. A significant diminution in photoluminescence (PL) emission of FM is evident in **Figure S4c** indicating a separated carrier and hole.

The production of ROS  $^1\text{O}_2$  and  $\cdot\text{O}_2$  are assessed using 1,3-diphenylisobenzofuran (DPBF) degradation, leading to a slump in absorbance at 410 nm<sup>[36]</sup> (**Figure 3a**) in the presence of ROS. With prolonged irradiation time, the absorption intensity falls steadily (**Figure 3c**), representing the continuous production of  $^1\text{O}_2$  by FMG under NIR. At the same time, the FM group generated more  $^1\text{O}_2$  than the FO and MX groups (**Figure 3b**), implying that the Schottky HJ formed at the interface of FO and MX improves electron-hole pair separation. A similar reduction of absorption intensity is observed for the FMG group, demonstrating capable photodynamic performance. The ability of FMG to produce  $\cdot\text{OH}$  under NIR was examined by comparing the absorbance of glucose-containing methylene blue (MB) solutions treated in different groups. MB was applied as the  $\cdot\text{OH}$  trapping agent in the presence of  $\text{H}_2\text{O}_2$ , which will react with  $\cdot\text{OH}$  to reduce the absorption intensity between 625 and 665 nm (**Figure 3d**).<sup>[37]</sup> As seen in **Figure 3e**, the FMG group exhibited the lowest absorbance at 652 nm, followed by the FM group, while the absorbance of the FO and MX groups displayed essentially little drop in comparison to the PBS group. From the corresponding quantitative analysis (**Figure 3f**), it is found that the decrease in absorbance in the FMG group is significantly greater than in the other groups. As NIR hastens the steady release of  $\text{Fe}^{3+}$  over time (**Figure S4d**), we believe that the elevated  $\cdot\text{OH}$  is primarily attributed to two factors: the photodynamic effect of FMG produces

$\text{H}_2\text{O}_2$ , which is then catalyzed to  $\cdot\text{OH}$  by  $\text{Fe}^{3+}$ , while the GOx in FMG catalyzes the oxidation of glucose in the solution to produce  $\text{H}_2\text{O}_2$  as well, further producing  $\cdot\text{OH}$ . Additionally, electron spin resonance (ESR) was applied to analyze the generation of  $^1\text{O}_2$  and  $\cdot\text{OH}$  by 2,2,6,6-tetramethylpiperidine-1-oxyl (TEMP) and 5,5-dimethyl-1-pyrroline N-oxide (DMPO). Under 808 nm NIR irradiation, TEMP- $^1\text{O}_2$  is detected with a typical 1:1:1 signal (**Figure S4e**), and **Figure S4f** depicts the four typical  $\cdot\text{OH}$  peaks with a ratio of 1:2:2:1. The intensity rises with prolonged NIR light irradiation time, indicating that  $^1\text{O}_2$  and  $\cdot\text{OH}$  are substantially generated, in agreement with the DPBF and MB results mentioned above.

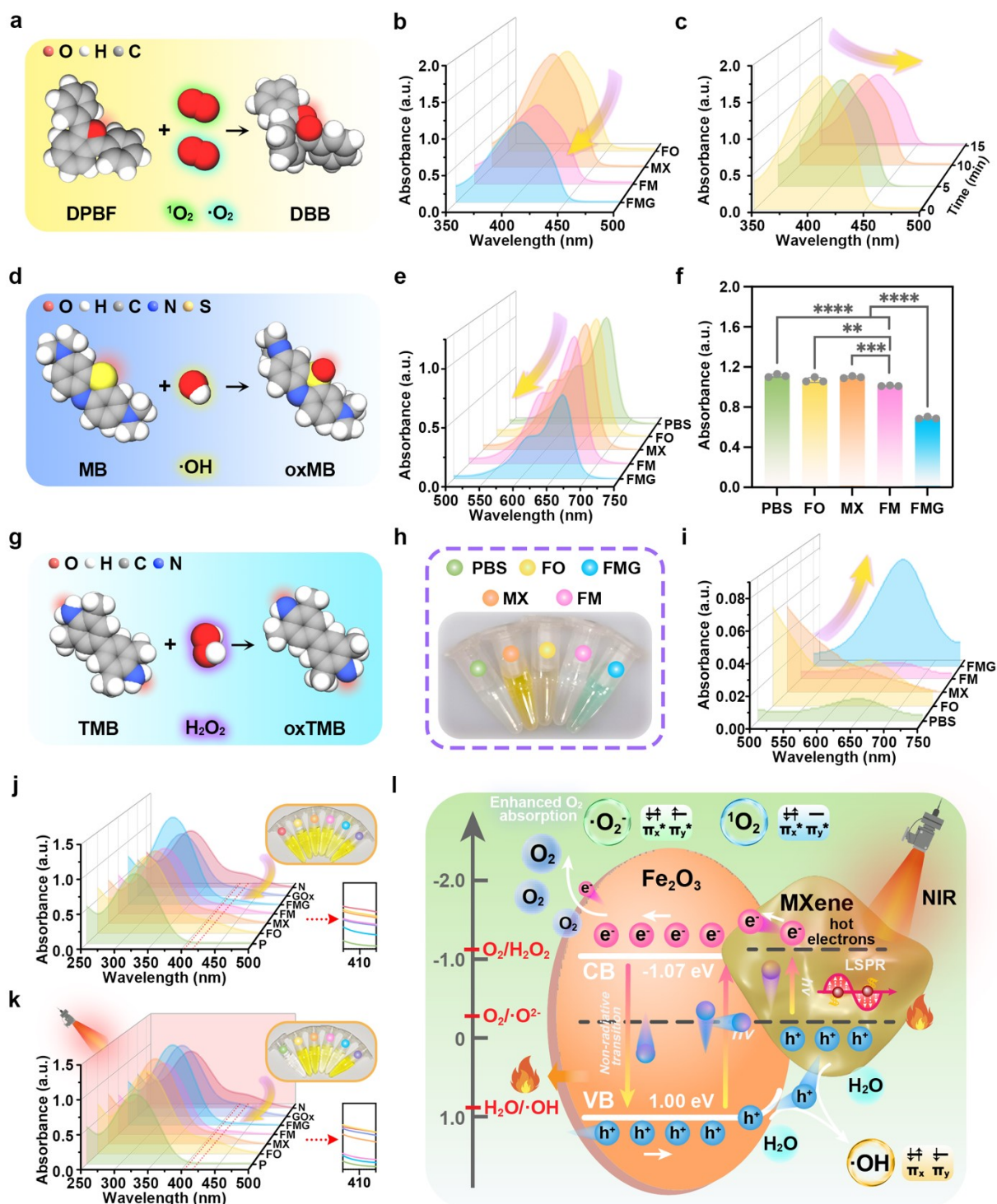


**Figure 3. Photodynamic performance of bio-HJs.** (a) Chemical reaction diagram of DPBF oxidation. (b) Absorption spectra of DPBF reduction of FO, MX, FM, and FMG under NIR irradiation, and (c) absorbance spectra of FM with varying irradiation times. (d) Chemical reaction between MB and

·OH. (e) Related spectra and (f) absorbance at 660 nm of MB solution co-cultured with different samples for 15 min under NIR irradiation. (g) Reaction mechanism of TMB with  $\text{H}_2\text{O}_2$ . (h) Color changes of TMB solutions with different treatments and (i) related absorbance spectra of TMB consumption under NIR irradiation. GSH consumption treated with PBS (named as “N”), FO, MX, FM, FMG, GOx, and  $\text{H}_2\text{O}_2$  (named as “P”) (j) without or (k) with NIR irradiation. (l) Schematic diagram of PDT effect mechanism of FM HJ. (Data are presented as mean  $\pm$  SD. Significance between two groups was calculated using one-way ANOVA and Tukey’s multiple comparisons test (f).  $n = 3$ . \* $p < 0.05$ , \*\* $p < 0.01$ , \*\*\* $p < 0.001$ , \*\*\*\* $p < 0.0001$ .)

To further investigate the existence of  $\text{H}_2\text{O}_2$ , 3,3',5,5'-tetramethylbenzidine (TMB) is applied to react particularly with  $\text{H}_2\text{O}_2$ , and the resultant product, TMB-ox, exhibits pronounced absorption at 652 nm and the solution changes from colorless to blue (**Figure 3g**).<sup>[38]</sup> As the results shown in **Figure 3h**, the solution of the FO group appears light yellow, while the solution of the FMG group appears light blue. Accordingly, the FMG and FO groups show significant absorption at 652 nm, whereas the other groups exhibit approximately equivalent absorption (**Figure 3i**). We assume that the absorption of FO results from residual FO nanoparticles that were not removed by centrifugation. The quantification results (**Figure S4g**) show that the absorbance of the FMG group is much higher than the absorbance of the other groups, demonstrating that FMG has the capacity to induce the production of  $\text{H}_2\text{O}_2$  from glucose.

Glutathione (GSH), a “self-defense system” in bacteria, resists extraneous oxidative stress,<sup>[39,40]</sup> however, as ROS accelerate GSH consumption, this antioxidant effect is broken down. Interestingly, the depletion of GSH is low for all groups of materials without glucose and NIR irradiation (**Figure S4h**). Although  $\text{Fe}^{3+}$  is highly oxidizing, it requires medium or short-wavelength light excitation to initiate reactivity. Thus, we add 5 w/v% glucose to the GSH solution, and the GSH consumption is examined under both dark and light conditions (**Figure 3j, k**). The addition of glucose resulted in the greatest GSH consumption of FMG under both dark and light conditions due to the oxidation of glucose to gluconate and  $\text{H}_2\text{O}_2$ , catalyzed by GOx under oxygenated conditions.  $\text{Fe}^{3+}$  also catalyzes the disproportionation of  $\text{H}_2\text{O}_2$  to produce  $\text{H}_2\text{O}$  and  $\text{O}_2$ , further increasing glucose oxidation. Comparing the amount of GSH depletion with or without NIR irradiation, it is observed that NIR only

enhances GSH consumption in FM-containing samples, likely as a result of the wide band gap of FO and the hot electrons of MX.

Last but not least, to explore the photodynamic mechanism and charge transfer process of our bio-HJs, the XPS valence band spectra (**Figure S4i**) of the various materials were measured. Based on the Kubelka–Munk function, the band-gap energy ( $E_g$ ) of FO is calculated to be 2.07 eV (versus NHE), which is the intercept of the curve's linear region extrapolated to the X-axis in its Tauc plot. According to the valence band spectrum of FO, the top of the valence band is estimated to be at 1.00 eV (versus NHE). Subsequently, the bottom of the conduction band is predicted to be at  $-1.07$  eV (versus NHE). The heterojunction formed at the interface of FO and MX imbues the bio-HJ FMG with favorable metallic and charge-carrier transfer properties, similarly seen in other MXene-based HJs (such as  $\text{Ti}_3\text{C}_2$ -MXene).<sup>[41]</sup> Taken together, F-bio-HJ possesses robust photodynamic and chemodynamic effects in a high-glucose environment, producing  $\text{Fe}^{3+}$ ,  $\cdot\text{O}^{2-}$ ,  $\cdot\text{OH}$ , and  $\text{H}_2\text{O}_2$ , as well as consuming GSH under 808 nm NIR irradiation.

From energy band structure analysis and DFT calculations (Supporting Results 2.2 and **Figure S6, 7**), it is evident that FM is a typical type II Schottky HJ.<sup>[42,43]</sup> The mechanism of the photothermal and photodynamic properties of FM is illustrated in **Figure S5g** and **Figure 3I**. Since MX has a lower work function than FO, electrons migrate from MX to FO at interfacial contact points. Upon equilibrium between two Fermi levels, the redistribution of charge results in the development of an intrinsic electric field at the interface, establishing a Schottky barrier between MX and FO. Nevertheless, the localized surface plasmon resonance (LSPR) recession generates active electrons with energies higher than the Schottky barrier, transferring them onto the adjacent FO and aiding the separation of electron-hole pairs. Moreover, some excited photogenerated electrons return to the holes *via* a non-radiative transition to accomplish electron-hole recombination and simultaneously create heat. Under NIR irradiation, high-energy hot electrons in MX are carried over the heterogeneous interface to the conduction band of FO, where they subsequently react with the oxygen adsorbed on the surface of the heterostructure to create ROS such as  $\cdot\text{OH}$  and  $^1\text{O}_2$ . The photogenerated ROS and heat may then disseminate and eradicate nearby bacteria by disintegrating cytoderm, altering the membrane permeability, and disrupting the structure of biological macromolecules, such as GSH, DNA, as well as proteins.

### 2.3. Anti-extracellular-bacterial assessment *in vitro*

This article is protected by copyright. All rights reserved.

Benefitting from the compelling photothermal, photodynamic, chemodynamic properties and GSH depletion property under NIR irradiation, F-bio-HJ is expected to possess hefty antibacterial infection potential. Initially, the anti-extracellular ability of F-bio-HJ was assessed against Gram-positive *S. aureus* and Gram-negative *E. coli in vitro* by spread plate method, Live/Dead assay, SEM, as well as leaking DNA and protein detection. As shown in **Figure 4a and c**, for FO, MX and FM groups, a large number of colonies is observed 10 min after culture in the dark, and the corresponding antimicrobial efficiency is low (**Figure 4b, d**). In contrast, the FMG group reaches more than 30% antimicrobial efficiency even without NIR, which is attributed to the cascade reaction induced by GOx to produce highly cytotoxic  $\cdot\text{OH}$ . After NIR irradiation for 10 min, a vast amount of bacteria remain on the plate of the FO group, whose antibacterial rates are only  $-11.5 \pm 11.7\%$  (*E. coli*) and  $19.5 \pm 0.9\%$  (*S. aureus*), implying that FO has barely any antibacterial ability. However, the bacterial colonies in MX, FM, and FMG groups are significantly decreased. The MX group achieves almost 100% antibacterial rate against *E. coli* and *S. aureus* due to its excellent photothermal ability to raise the temperature to nearly  $70\text{ }^{\circ}\text{C}$  (**Figure S5a, b**); however, harm to normal tissues by this high temperature should be considered. Regarding the FM group, the antibacterial rates are  $74.4 \pm 4.7\%$  (*E. coli*) and  $85.8 \pm 5.4\%$  (*S. aureus*) with the help of NIR irradiation, while for FMG these rates  $99.0 \pm 0.3\%$  (*E. coli*) and  $97.8 \pm 0.6\%$  (*S. aureus*). Although the photothermal ability of FM is better than that of FMG, the antimicrobial ability of FMG with NIR irradiation is better due to the extra chemodynamic effect brought by GOx. Under NIR irradiation, a combination of photothermal local warming and photo/chemodynamic generation of ROS in high glucose microenvironment endows F-bio-HJ with a significant killing effect on extracellular *S. aureus* and *E. coli*.

A qualitative analysis of the antibacterial efficiency of each group was conducted using the Live/Dead staining assay. As shown in **Figure 4e**, without NIR irradiation, the red fluorescence of dead bacteria is only slightly obvious in *S. aureus* treated with FMG, and the green fluorescence of living bacteria is predominant in the rest of the groups, indicating F-bio-HJ can possess some bactericidal ability even without NIR. After NIR irradiation for 10 min, the PBS and FO groups exhibit similar green fluorescence. By striking comparison, the MX group exhibits copious red fluorescence due to its excessively powerful photothermal effects, the FM group shows yellow fluorescence (overlay of green and red), while the FMG group exhibits a stronger red fluorescence, consistent with the above results.

Afterward, the morphology and membrane integrity of *E. coli* and *S. aureus* after treatment are evaluated by SEM. Obviously, the bacteria in the PBS and FO groups all display characteristic and integrated rod (*E. coli*) or spherical (*S. aureus*) morphology (**Figure 4f**). In groups treated with MX, *S. aureus* with integrated cellular morphology and *E. coli* with only a few wrinkles (green arrows) on the surface are observed after incubation in darkness, while those exposed to NIR undergo more surface folding, shrinkage, and even cracking. In the FM group, *S. aureus* and *E. coli* cell membranes show significant wrinkling and cytoplasmic leakage only when illuminated by NIR light. In contrast, bacteria cultured with FMG bio-HJs demonstrate the most severe morphological malformation and oozing of cellular content. Moreover, we evaluate the extent of damage to the bacterial cell membrane by measuring the quantity of DNA and protein exuded. As shown in **Figure 4g and h**, the amount of protein and DNA exudation from MX, FM, and FMG groups under NIR irradiation is higher than that of the corresponding group in the dark; this confirms that these materials damage the bacterial cell membrane structure and change the permeability of bacterial cell membrane with the help of NIR irradiation, in agreement with the cytoplasmic exudation observed in SEM. In conclusion, these results are congruent with the previous results, affirming that local hyperthermia and ROS produced by F-bio-HJ can efficiently damage the phospholipid bilayers of the bacterial membrane and impair cell membrane permeability, resulting in the rapid leaking of cellular matrix under NIR.

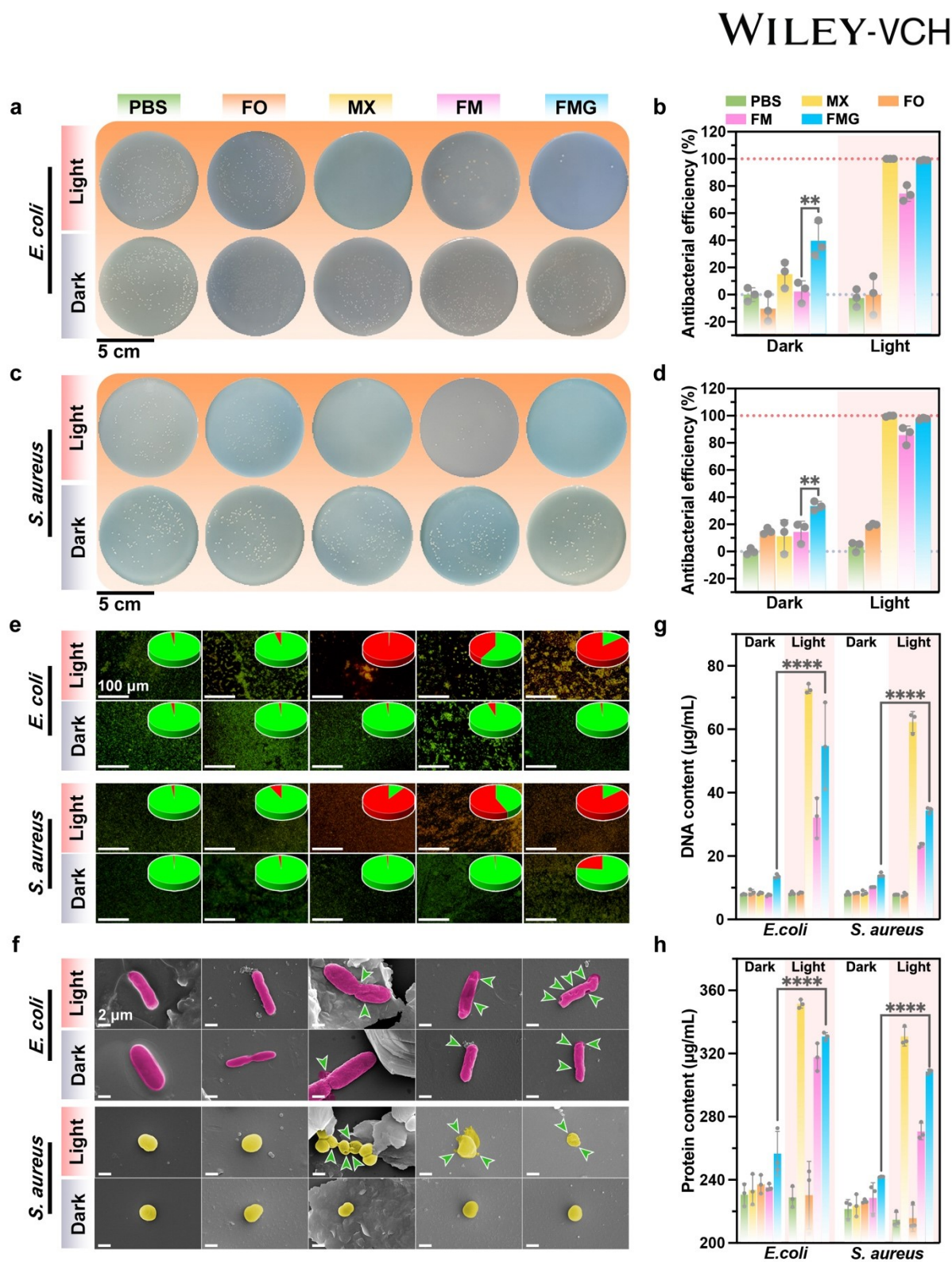


**Figure 4. Anti-extracellular-bacterial performance of bio-HJs *in vitro*.** Images of bacterial colonies of (a) *E. coli* and (c) *S. aureus* treated with different materials and (b, d) the corresponding antibacterial rate. (e) Live/Dead staining of *S. aureus* and *E. coli* with PBS, FO, MX, FM, and FMG in dark or NIR

irradiation. (f) Micro-morphology of *S. aureus* and *E. coli* characterized by SEM after contact with PBS, FO, MX, FM, and FMG with or without NIR irradiation (green arrows mark the shrinking and damaged cell membranes). (g) The DNA and (H) protein content of *S. aureus* and *E. coli* leaked in the supernatant after different treatments with or without NIR irradiation. (Data are presented as mean  $\pm$  SD. Significance between two groups was calculated using one-way ANOVA and Tukey's multiple comparisons test (b, d, g, h).  $n = 3$ . \* $p < 0.05$ , \*\* $p < 0.01$ , \*\*\* $p < 0.001$ , \*\*\*\* $p < 0.0001$ .)

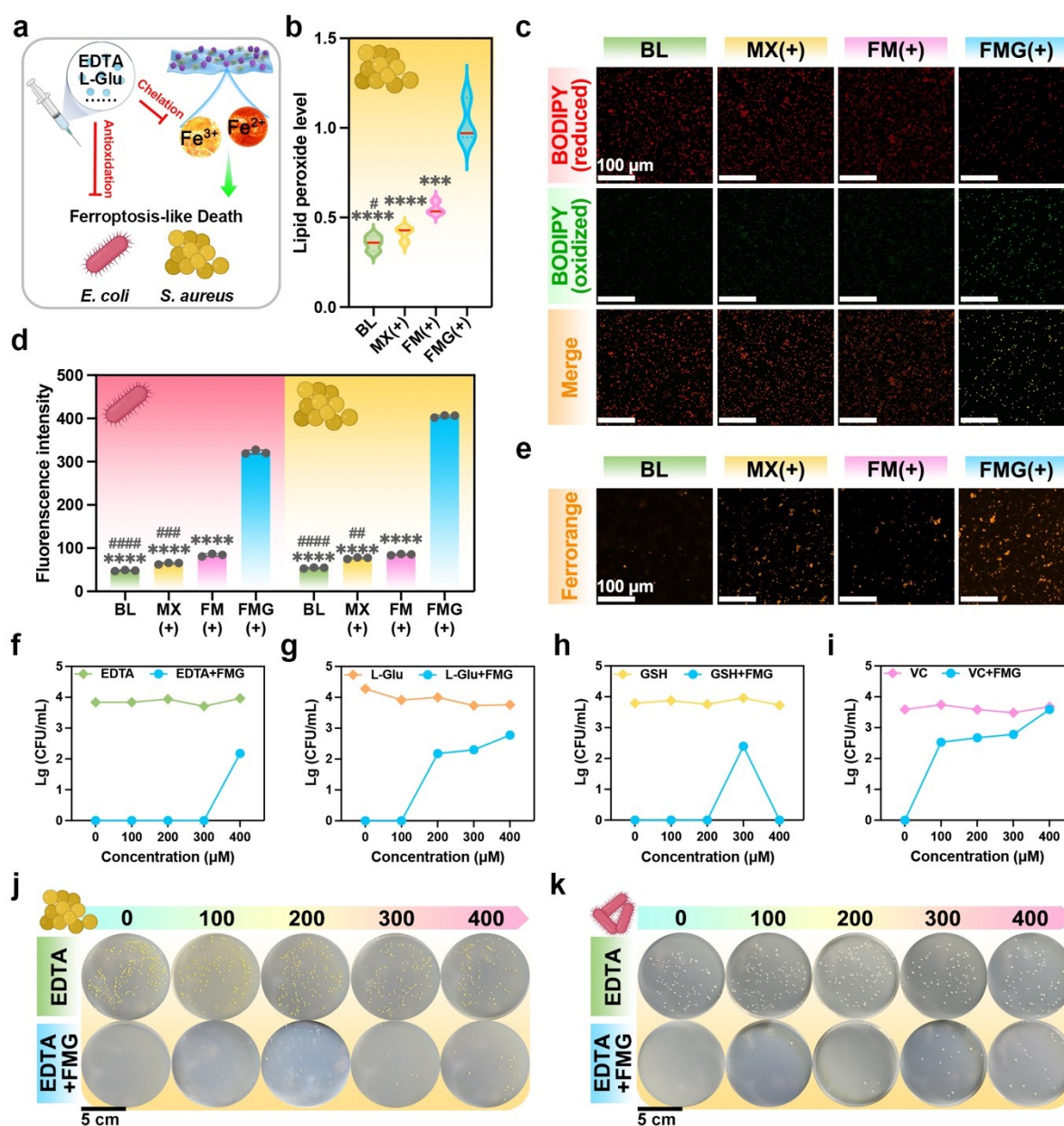


**Figure 5. The antibacterial property of F-bio-HJ via ferroptosis.** (a) Schematic illustration of mechanism validation. (b) Lipid peroxide level in *S. aureus* with PBS, MX, FM, and FMG under NIR irradiation. (c) Lipid peroxidation induced by PBS, MX, FM, and FMG in *S. aureus* under NIR irradiation and (d) the associated quantified fluorescence intensity in *E. coli* and *S. aureus*. Lipid peroxide was detected using a BODIPY581/591-C11 probe. (e)  $\text{Fe}^{2+}$  level in *S. aureus* with different treatments under NIR irradiation. The  $\text{Fe}^{2+}$  level was visualized by Ferrorange probe. (f) EDTA, (g) L-Glu, (h) GSH, and (i) VC inhibit the antibacterial property of FMG. Photograph of culture plates of (j) *S. aureus* and (k) *E. coli* treated with EDTA and FMG under NIR irradiation. (Data of (b) are presented as violin plot (median as red line, quartiles as dotted lines). Data of (d) are presented as mean  $\pm$  SD. Significance between two groups was calculated using one-way ANOVA and Tukey's multiple comparisons test (b, d).  $n = 3$ . \* and # represent  $p < 0.05$  when compared with FMG and FM, respectively. \* $p < 0.05$ , \*\* $p < 0.01$ , \*\*\* $p < 0.001$ , \*\*\*\* $p < 0.0001$ .)

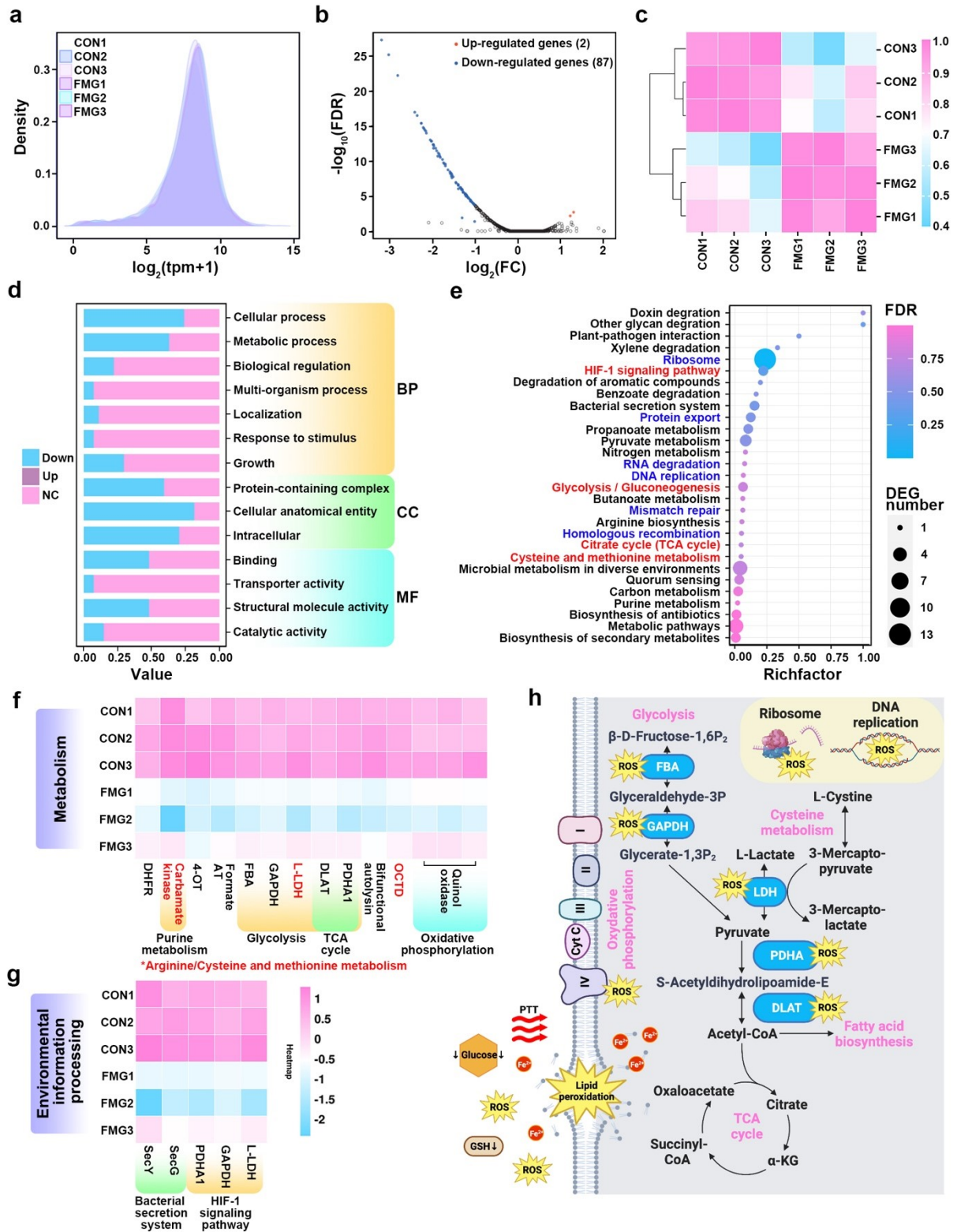
We next explore the mechanism of the high potency and rapid bacterial killing ability of F-bio-HJ. Excessive ROS ( $\text{H}_2\text{O}_2$ ,  $\cdot\text{OH}$ ,  $^1\text{O}_2$  and  $\cdot\text{O}_2^-$ ) can break the intrabacterial redox equilibrium, denature the proteins and nucleic acids, and impair the bacterial membrane,<sup>[42]</sup> thus, we first detect the intracellular ROS in treated bacteria. As shown in **Figure S8**, there is almost no green fluorescence signal (ROS) in the PBS group, indicating a low level of intra-bacterial ROS. However, the signal is even weaker in the MX group, demonstrating that despite excellent heating capabilities, MX cannot raise the intra-bacterial ROS level. In contrast, bacteria treated with FO, FM, and FMG exhibit an appreciable increment in intracellular ROS level. Among them, the fluorescence intensity of ROS in the FMG group is significantly the highest, which is beneficial for disrupting the intracellular structure of bacteria and making them easier to eliminate. This reveals that F-bio-HJ-treated bacteria can be attacked both internally and externally by ROS generated in the photodynamic and chemodynamic processes.

#### 2.4. F-bio-HJ induces ferroptosis in extracellular bacteria

In addition to the hyperthermal effect and extra-intracellular ROS attack,  $\text{Fe}^{2+}$  is another aggressor contributing to the outstanding antibacterial effect of the FMG bio-HJs. While the antibacterial capability of ROS has been widely recognized,  $\text{Fe}^{2+}$  and  $\text{Fe}^{3+}$  have just recently been proven to kill

bacteria *via* ferroptosis-like death.<sup>[16]</sup> Therefore, we also examined whether FMG bio-HJs cause ferroptosis in bacteria (**Figure 5a**). As shown in **Figure 5b and c**, lipid peroxidation occurs the most in *S. aureus* treated with FMG under NIR irradiation, followed by FM. There is barely any lipid peroxidation observed in the MX and BL group. Further, higher quantities of Fe<sup>2+</sup> were accumulated in both *E. coli* and *S. aureus* treated with FMG with NIR illumination (**Figure 5d, e**), which is a typical signature of ferroptosis.

To validate these results, a ferroptosis inhibitor, ethylenediaminetetraacetic acid (EDTA), was added.<sup>[16]</sup> EDTA chelation of iron was found to alleviate bacterial killing significantly, indicating that FMG's antibacterial properties are hindered without the action of free iron (**Figure 5f, j, k, Figure S9a, e, f**). Other iron-binding reagents, such as L-glutamate (L-Glu), also impacted the antibacterial activity of FMG (**Figure 5g, Figure S9b, e, f**). Antioxidants like GSH and vitamin C (VC) also inhibit the antibacterial activity of FMG (**Figure 5h, i, Figure S9c, d, e, f**). We further found that EDTA and L-Glu suppressed lipid peroxidation induced by FMG and FM according to the malondialdehyde (MDA) content in *S. aureus* (**Figure S10**). These findings indicate that compounds that chelate iron, lessen lipid peroxidation, and prevent oxidation limit the bactericidal activity of F-bio-HJ.



This article is protected by copyright. All rights reserved.

**Figure 6. Exploration of anti-extracellular-bacterial mechanisms of F-bio-HJs by RNA-seq analysis.**

(a) tpm distribution for all samples. (b) Volcano plots of DEGs. (c) Correlation analysis of all samples. (d) The DEGs in CON versus FMG by GO enrichment terms. BP: biological process; CC: cellular component; MF: molecular function. (e) KEGG enrichment for the DEGs. (f) Heatmap of DEGs in the metabolism pathway. (g) Heatmap of DEGs in the environmental information processing pathway. (h) Schematic illustration of anti-extracellular-bacterial mechanisms of FMG bio-HJs.

To further verify the detailed mechanism, we conducted RNA-seq analysis on *S. aureus* treated with FMG bio-HJs under NIR irradiation. As shown in **Figure 6 a-c**, FMG bio-HJs impacted the expression of 3.47 % of genes in *S. aureus*. According to gene ontology (GO) enrichment analysis, all terms (biological process, cellular component, and molecular function) were down-regulated (**Figure 6d**). All cellular components were damaged and metabolic processes were significantly disrupted, including peptide, protein, amide, and macromolecule metabolism. KEGG pathway enrichment results show that metabolism was remarkably affected, including the citrate cycle (TCA cycle), cysteine and methionine metabolism, arginine biosynthesis, glycolysis, nitrogen metabolism, and others (red terms in **Figure 6e**). Additionally, genetic processes (blue terms in **Figure 6e**) including ribosome, DNA replication, RNA degradation, and mismatch repair were severely impacted by FMG bio-HJs. Interestingly, the hypoxia-inducible factor 1 (HIF-1) signaling pathway was also enriched in KEGG, indicating that bacteria's oxygen consumption was affected. Combined with the enrichment of the oxidative phosphorylation pathway, it is possible that cytochrome c oxidase (Complex IV in the respiratory chain) was inhibited by FMG bio-HJs. The heatmap of differentially expressed genes (DEGs) further demonstrated that most genes were significantly downregulated in pathways in metabolism and environmental information processing (HIF-1 signaling pathway and bacterial secretion system) (**Figure 6f, g**).

To summarize, we have proposed the anti-extracellular-bacterial mechanism of F-bio-HJ (**Figure 6h**): with NIR, F-bio-HJ first brings local heat and generates a profusion of ROS ( $\cdot\text{O}^2$ ,  $\text{H}_2\text{O}_2$ ,  $\cdot\text{OH}$ , etc.) to break the bacterial membrane structure. Meanwhile, GOx consumes  $\text{O}_2$  to convert glucose into gluconic acid and  $\text{H}_2\text{O}_2$ , blocking the subsequent energy supply to the bacteria. Then,  $\text{Fe}^{3+}$  consumes GSH under acidic conditions and catalyzes the production of  $\cdot\text{OH}$  from  $\text{H}_2\text{O}_2$  to damage the internal structures and external membrane of bacteria, resulting in cytoplasmic extravasation, GSH

deficiency, and reduction to  $\text{Fe}^{2+}$ . With the simultaneous accumulation of intra-bacterial ROS and  $\text{Fe}^{2+}$ , severe lipid peroxidation results in irreversible ferroptosis of bacteria. The metabolic processes associated with glucose, lipids, cysteine, purine, and  $\text{O}_2$ , as well as genetic processes, all appear disrupted and implies an overall dysfunction of bacteria. These results indicate that F-bio-HJ is capable of eliciting bacterial mortality effectively and rapidly with similar hallmarks to ferroptosis, strongly suggesting the existence of ferroptotic damage on extracellular bacteria.

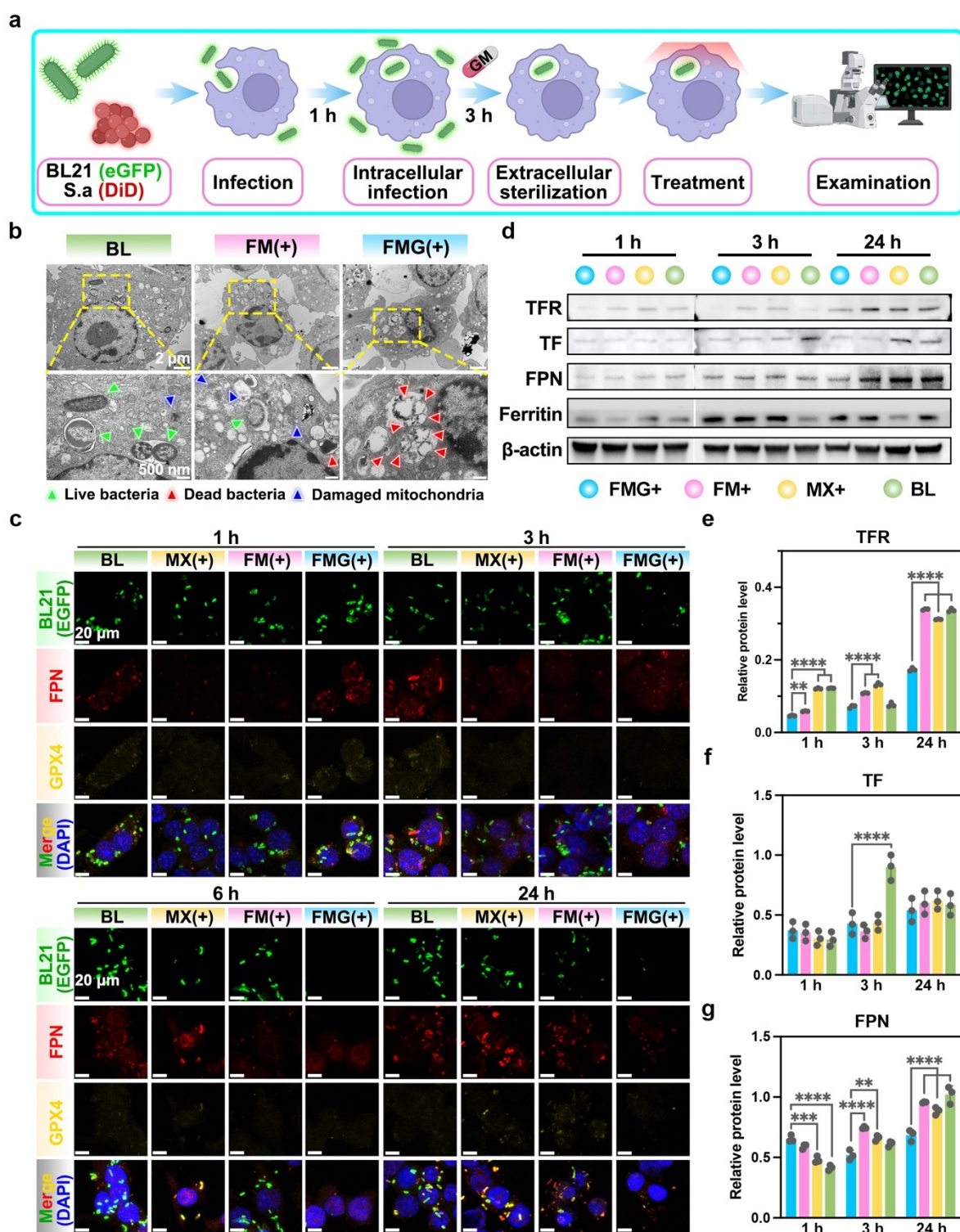


**Figure 7. Intracellular antibacterial property.** (a) Schematic illustration of intracellular antibacterial property evaluation. (b) TEM characterization of intracellular *E. coli* treated by PBS, FM, and FMG

under NIR irradiation. (c) Confocal imaging of *E. coli* (EGFP-BL21, green) with FPN (red) and GPX4 (yellow) immunofluorescence staining in RAW264.7 macrophages with different treatments after 1, 3, 6, and 24 h. DAPI stained cell nucleus (blue). (d) Western Blot of TFR, TF, FPN, and ferritin protein expression in RAW264.7 cells. The grey scale statistics of (e) TFR, (f) TF, and (g) FPN. (Data are presented as mean  $\pm$  SD. Significance between two groups was calculated using one-way ANOVA and Tukey's multiple comparisons test (e-g).  $n = 3$ . \* $p < 0.05$ , \*\* $p < 0.01$ , \*\*\* $p < 0.001$ , \*\*\*\* $p < 0.0001$ , ns: no significance.)

## 2.5. F-bio-HJ assists intracellular bacteria-targeted ferroptosis

For any therapeutic agent, it is mandatory to verify the latent cytotoxicity of nanomaterials prior to their utilization in biological applications.<sup>[44]</sup> We have demonstrated that our bio-HJs have excellent biocompatibility and even the potential of improving healthy cell proliferation and migration *via* LIVE/DEAD staining, CCK-8, cytoskeleton staining, and scratch assay on L929 fibroblasts and HaCaT keratinocytes (Supporting Results 2.3, **Figure S11-13**). Recent research has proven that ferroptotic stress promotes the capacity of macrophages against intracellular bacteria.<sup>[15]</sup> Therefore, we examined whether F-bio-HJ assists RAW 264.7 macrophages in killing intracellular bacteria (**Figure 7a**). Initially, TEM characterization of intracellular *E. coli* treated by FMG and FM with NIR was conducted. Compared to the blank control group (BL), FMG treatment decreased the amount of intracellular *E. coli* with obviously disrupted structures (**Figure 7b**). In contrast, a decreased number of dead bacteria and an increase in intracellular bacteria with intact morphology can be observed in the FM group. Furthermore, damaged mitochondria are found in both FM and BL groups, indicating potential cell dysfunction. These results demonstrated that FMG bio-HJs effectively assist intracellular antibacterial viability without harming cells.

To corroborate the mechanism of precise intracellular sterilization, we investigated the co-localization of GPX4 and FPN with internalized bacteria. As seen in **Figure 7c**, 1h after FMG, FM, MX and blank control (BL) treatment to infected cells, FPN (red) and intracellular BL21 (green) exhibited evident co-localization, particularly in the FMG group. After 3 h, the number of internal bacteria in the FMG group dropped, followed by the full removal of BL21 after 6 h, which is consistent with the results of TEM. However, after treatment with FM or MX, FPN expression did not begin to rise for at

least 3 h (**Figure S14a**). Still, FPN expression remained high surrounding intracellular bacteria in the BL group, probably due to inadequate  $\text{Fe}^{2+}$  supply in the face of severe infection. After 24 h, there is a significantly lower level of FPN in infected macrophages treated with FMG bio-HJs under NIR irradiation, implying faster sterilization and cell recovery. Concomitantly, the expression of GPX4 was elevated in the first hour following FMG treatment and continued to decline thereafter (**Figure S14b**). In the BL group, GPX4 expression began to diminish 6 h after infection. In contrast, the FM and MX groups express GPX4 at a greater level after 24 h. Therefore, through co-localization of FPN and GPX4 with intracellular BL21, we found that F-bio-HJ can effectively assist macrophages in destroying intracellular bacteria by transducing ferroptotic stress *via* FPN.

To further validate the effect of F-bio-HJs on ferroptosis in RAW264.7, we examined the expression of FPN<sup>[23]</sup>, transferrin receptor (TFR), transferrin (TF)<sup>[45]</sup>, and ferritin<sup>[46]</sup>. As shown in **Figure 7d-g**, after 3 h post-treatment, FMG(+) and FM(+) groups exhibit a low expression of TFR and TF, two main transporters of  $\text{Fe}^{3+}$ , likely due to a sufficient supply of  $\text{Fe}^{2+}$  for macrophages. Ferritin, a protein for  $\text{Fe}^{2+}$  storage,<sup>[46]</sup> demonstrates more ferrous accumulation in the FMG(+) group, denoting that ferroptosis can occur earlier in this treated group. Meanwhile, the expression of FPN increased due to the  $\text{Fe}^{2+}$  accumulation in FMG(+), FM(+) and MX(+) groups after 3 h. However, the specific mechanism by which ferroptotic and oxidative stress created by FMG avoids damaging normal cells should be further explained to understand the accelerated antibiosis process and cutaneous tissue regeneration.

## 2.6. F-bio-HJ induces “hunger protection” against ferroptosis in cells

To determine whether F-bio-HJ protects cells from ferroptosis while assisting in intracellular antibacterial activity, lipid peroxidation was evaluated in bacteria-infected macrophages. As shown in **Figure 8a and b**, FM increases lipid peroxidation in *S. aureus*-infected RAW264.7 cells by more than thrice and twofold, while FMG induces no lipid peroxidation. The MX group shows a slightly lower lipid peroxidation level. Nevertheless, the concentration of  $\text{Fe}^{2+}$  accumulated in cells does not show significant differences among groups (**Figure 8c, d**). Moreover, lower lipid peroxidation (**Figure S15**), MDA (**Figure S16**), and  $\text{Fe}^{2+}$  (**Figure S17**) levels are observed in L929 and HaCaT cells 24 h after being treated with FMG. Therefore, we hypothesized that the action of GOx may be part of the key to the cell protection mechanism.

Generally, normal cells have an innate anti-ferroptosis system, such as system  $x_c^-$  cystine-GSH-GPX4 axis. Facing ferroptotic stress, normal cells passively protect themselves by expressing more SLC7A11 and GPX4. However, SLC7A11/xCT was not expressed enough in RAW264.7 cells (**Figure 8e, f**), thus RAW264.7 is a cell line with a low basal SLC7A11/xCT expression. The previous study has demonstrated that under energy stress, AMPK plays a causal role in ferroptosis resistance in cell lines with low SLC7A11/xCT level.<sup>[33]</sup> With the help of GOx, F-bio-HJ rapidly consumes extracellular glucose and actively creates a starvation environment, which is the trigger for active hunger protection pathways by cells. The phosphorylation of AMPK surged in RAW264.7 (**Figure 8e, g**), which is the cell's method to protect macrophages from ferroptosis. As a result, the inflammatory state was rapidly alleviated as the expression of IL-1 $\beta$  and TNF- $\alpha$  decreased in the FMG group after treatment (**Figure 8e, h, i**). Moreover, the innate protection ended earlier as RAW264.7 treated with FMG expressed lower GPX4 than other groups 3 h after treatment (**Figure 8e**). Conclusively, protection against cell ferroptosis and downstream inflammation is provided mostly by the activation of the AMPK signaling pathway (**Figure 8j**).

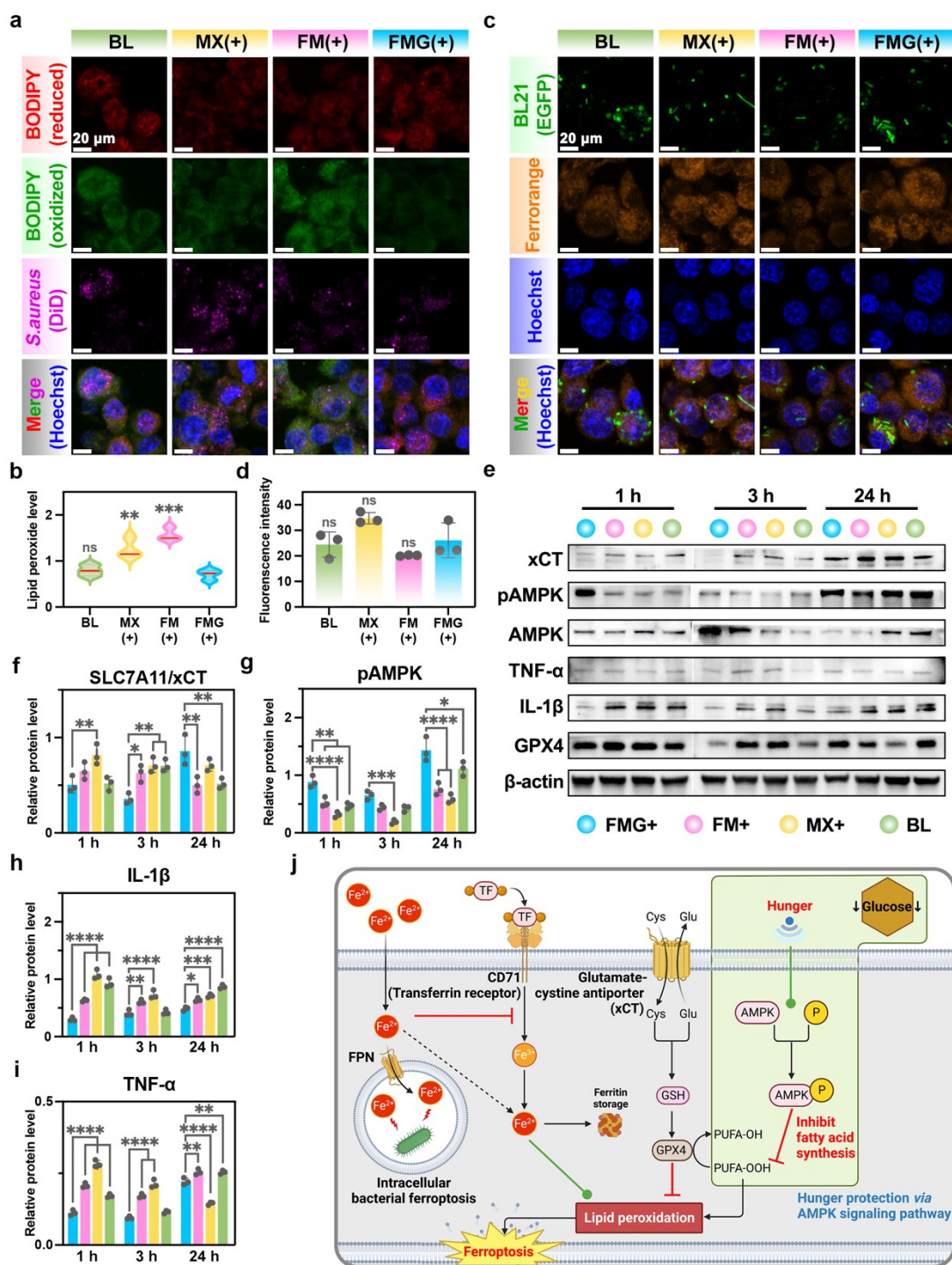


**Figure 8. Hunger-triggered protection in bacteria-invaded RAW264.7 cells.** (a) Confocal images of DiD-labeled *S. aureus* (pink) co-located with lipid peroxides visualized by BODIPY 581/591-C11 probe (red and green) with Hoechst 33342-stained cell nucleus (blue) and (b) the corresponding

quantitative lipid peroxide level. (c) Confocal images of Fe<sup>2+</sup> (FerroOrange probe, orange) co-located with BL21 (green) with Hoechst 33342-stained cell nucleus (blue) and (d) the corresponding quantitative Fe<sup>2+</sup> level (\* represent  $p < 0.05$  when compared with the FMG(+) group). (e-i) Immunoblotting of SLC7A11/xCT, pAMPK, AMPK, IL-1 $\beta$ , and TNF- $\alpha$  protein expression. (j) Scheme of hunger protection against ferroptosis. (Data of (b) are presented as violin plot (median as red line, quartiles as dotted lines). Other data are presented as mean  $\pm$  SD. Significance between two groups was calculated using one-way ANOVA and Tukey's multiple comparisons test (b, d, f, g, h, i).  $n = 3$ . \* $p < 0.05$ , \*\* $p < 0.01$ , \*\*\* $p < 0.001$ , \*\*\*\* $p < 0.0001$ , ns: no significance.)

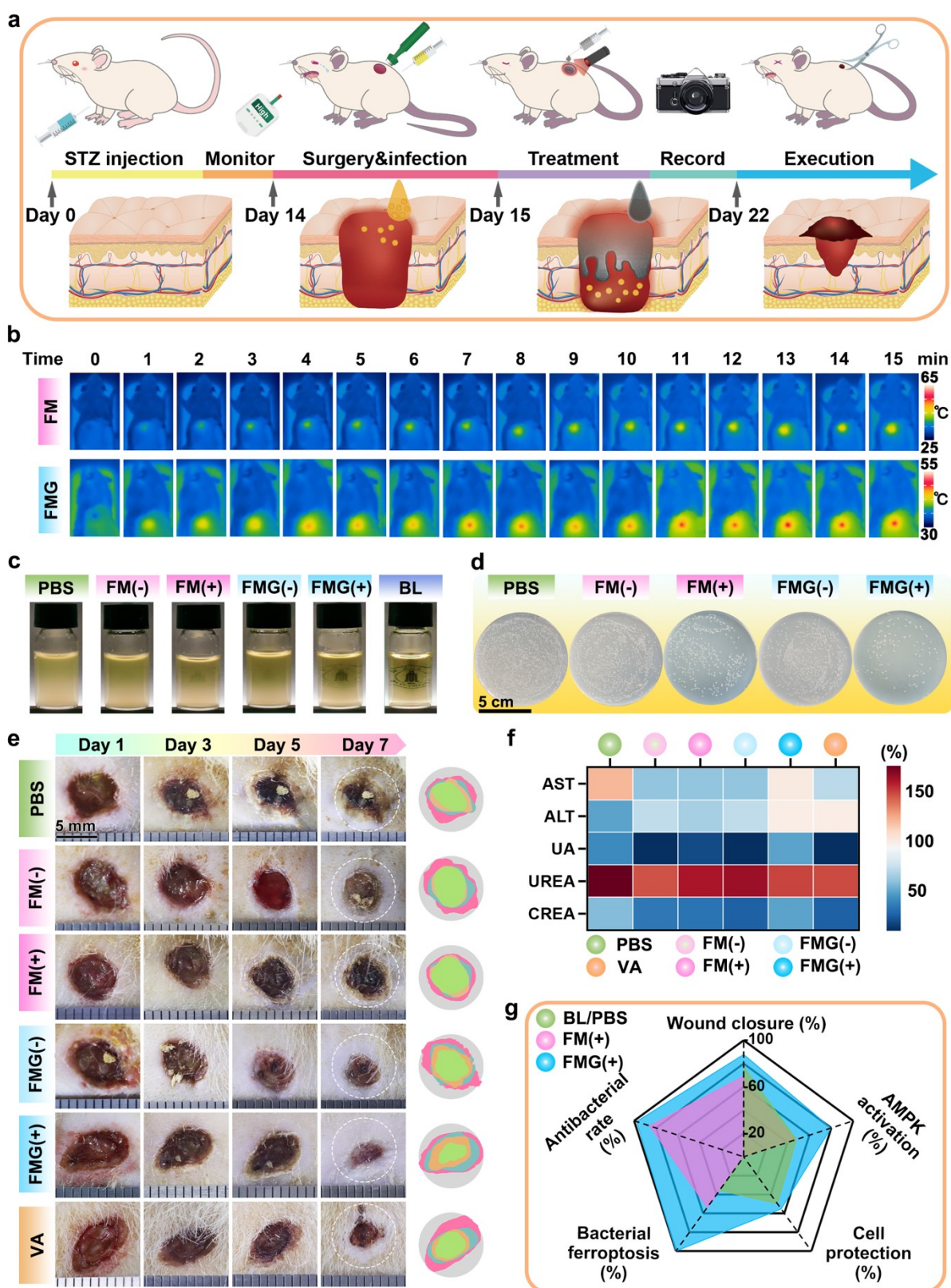


**Figure 9. Therapeutic assessment of F-bio-HJs *in vivo*.** (a) Graphical depiction of diabetic infectious wound establishment and therapeutic process on SD rats. (b) Infrared thermal photos under NIR irradiation (808 nm, 1.5 W·cm<sup>-2</sup>). Images of (c) turbid liquid and (d) bacterial colonies collected from the wound after treatment. (e) Photographs of the wound areas of rats with infected wounds treated differently. (f) The heatmap of serum biochemical indexes of rats on the sacrifice day. (g) Comprehensive performance of FMG, FM and BL/PBS control groups.

## 2.7. Antibacterial and tissue reconstruction *in vivo*

Considering the persuasive results of the bio-HJs' antibacterial ability and cytocompatibility *in vitro*, a full-thickness skin defect model was constructed in diabetic Sprague-Dawley (SD) rats<sup>[47]</sup> with *S. aureus* infection ( $1 \times 10^8$  CFU·mL<sup>-1</sup>) to evaluate the *in vivo* therapeutic efficacies of FMG treatment with NIR irradiation (FMG(+)) and without (FMG(-)), FM with NIR (FM(+)) and without (FM(-)), a positive control group (vancomycin, VA), and a negative control group (PBS). The construction of the infected diabetic wound model is illustrated in **Figure 9a**. The weight of rats indicates a downtrend (**Figure S18a**), and the blood glucose of all rats rose to at least 16.8 mmol·L<sup>-1</sup> on the second day after injection of streptozocin (STZ) (**Figure S18b**),<sup>[47]</sup> implying the successful establishment of a diabetes mellitus type 1 model.

On the treatment day (day 15), as the real-time infrared thermal images show in **Figure 9b**, the temperature of FMG and FM gradually rose to nearly 50°C within 7 min, which is consistent with the preliminary photothermal effect assessment. After phototherapy, bacteria from the wounds were collected and cultured in liquid and solid Luria-Bertani (LB) medium (**Figure 9c, d**), and the quantitative results were obtained. Both tests demonstrate that FMG bio-HJs with NIR irradiation possess the best antibacterial ability among the groups. Notably, to evaluate the antimicrobial efficacy of different groups in our *S. aureus*-induced infected diabetic wound, we also spread the wound exudate on the *S. aureus* selective chromogenic medium where only colonies of *S. aureus* exhibit a purple coloration (**Figure S19**). The results demonstrate the majority of bacteria present in the wound are *S. aureus*, and our F-bio-HJ possess the highest antimicrobial efficacy against *S. aureus*.

To assess the therapeutic ability of FMG bio-HJs, photographs of the skin wound were recorded at days 1, 3, 5, 7 after treatment (**Figure 9e**). The first day after treatment, the smallest wounds were observed in the FM(+) and PBS groups. The FMG(+) group displays similar wound closure rate with the VA group (**Figure S20a**). Interestingly, the differences gradually shrink and there are no significant differences among these groups on day 5, probably because of the scab covering the wound (**Figure S20b, c**). Finally, the infected wound in the FMG(+) group possesses the smallest wound size and is nearly entirely covered by regenerated skin on day 7 following therapy, indicating a fastest healing process among all groups. The quantitative results demonstrate that the final wound closure rate of the FMG(+) group is  $87.84 \pm 1.92\%$ , compared with  $80.11 \pm 2.30\%$  for VA group,  $78.82 \pm 1.53\%$  for FMG(-) group,  $69.09 \pm 0.83\%$  for FM(+) group,  $66.50 \pm 3.67\%$  for FM(-) group, and  $77.07 \pm 2.49\%$  for PBS group (**Figure S20d**). Comparatively, FMG bio-HJs attribute more to wound regeneration than FM because of the stronger PDT and CDT. The wound in the FMG(+) group exhibits superior healing than that in the FMG(-) group due to the potential pro-regenerative effect of PTT. Furthermore, the main organs (heart, kidney, liver, lung, and spleen) show no obvious damage or abnormality in Hematoxylin and Eosin (H&E) staining for all groups (**Figure S21**). Serum biochemical and blood routine indicators also show no significant differences among the groups (**Figure 9f, Figure S22, and Table. S1**). These results initially validate that FMG bio-HJs possess robust therapeutic efficacy without systemic toxicity to expedite the cutaneous regeneration of bacteria-invaded full-thickness wounds in a diabetic rat model.

To further evaluate the inflammatory response, collagen deposition, and angiogenesis efficiency of the different groups during the process of wound regeneration, skin tissues centered around the wound were collected upon sacrifice and analyzed with H&E, Masson's trichrome, Sirius red staining, and immunofluorescence staining. As shown in **Figure 10a-c**, the epidermal layers are thickened in all groups, but the wounds are incompletely healed, with the FMG(+) group being the closest to complete healing. In the PBS group, local congestion and poor wound healing can be observed. The VA group had an average degree of wound healing and thickness of the newborn epidermal layer, but a significantly lower amount of collagen fibers. In contrast, the FM(-) group had attenuated congestion, looser connective tissue, and poor wound healing. In the FM(+) group, neovascularization was boosted, but the new epidermal layer was thin, the connective tissue density increased slightly, and the degree of wound healing was better than that in the FM(-) group. In the FMG(-) group, the new epidermis was seen to increase compared with the FM group, but local

congestion was still seen, and the wound healing was average. In the FMG(+) group, there was an escalation in re-epithelialization and collagen synthesis, the structure of the skin layers was clear, and the wound was largely healed, resembling normal skin tissue. In addition, **Figure 10d** confirms the angiogenesis property of different materials: except in the FM(-) group, all other groups show a good amount of vascular endothelial growth factor (VEGF) (green) expression in new granulation tissue. Expression of CD31 (red) indicates neovascularization, which is highest in the FMG(+) group, followed by the FM(+) and VA groups.

As ferroptosis induced by FMG bio-HJs contributes to extracellular-antibacterial properties of the material and macrophage defense against intrusive bacteria *in vitro*, we investigated whether the same ferroptosis-associated bacterial eradication happens *in vivo*. Immunofluorescence staining of FPN, GPX4, and ferritin was conducted to evaluate the ferroptosis level in the wound (**Figure 10e and Figure S23**). The expression of FPN is drastically elevated in the FMG(+) group, implying the export of excessive  $\text{Fe}^{2+}$  from wound cells. Meanwhile, the staining intensity of both GPX4 and ferritin shows no significant difference in the PBS and FMG(+) groups, implying a low level of ferroptosis and a normal level of iron accumulated in cells on day 7. These results demonstrate that FMG coupled with NIR irradiation can efficiently accelerate re-epithelization, enhance collagen deposition, and bolster angiogenesis, resulting in the rapid healing of infected diabetic cutaneous wounds *via* a ferroptosis-mediated mechanism.

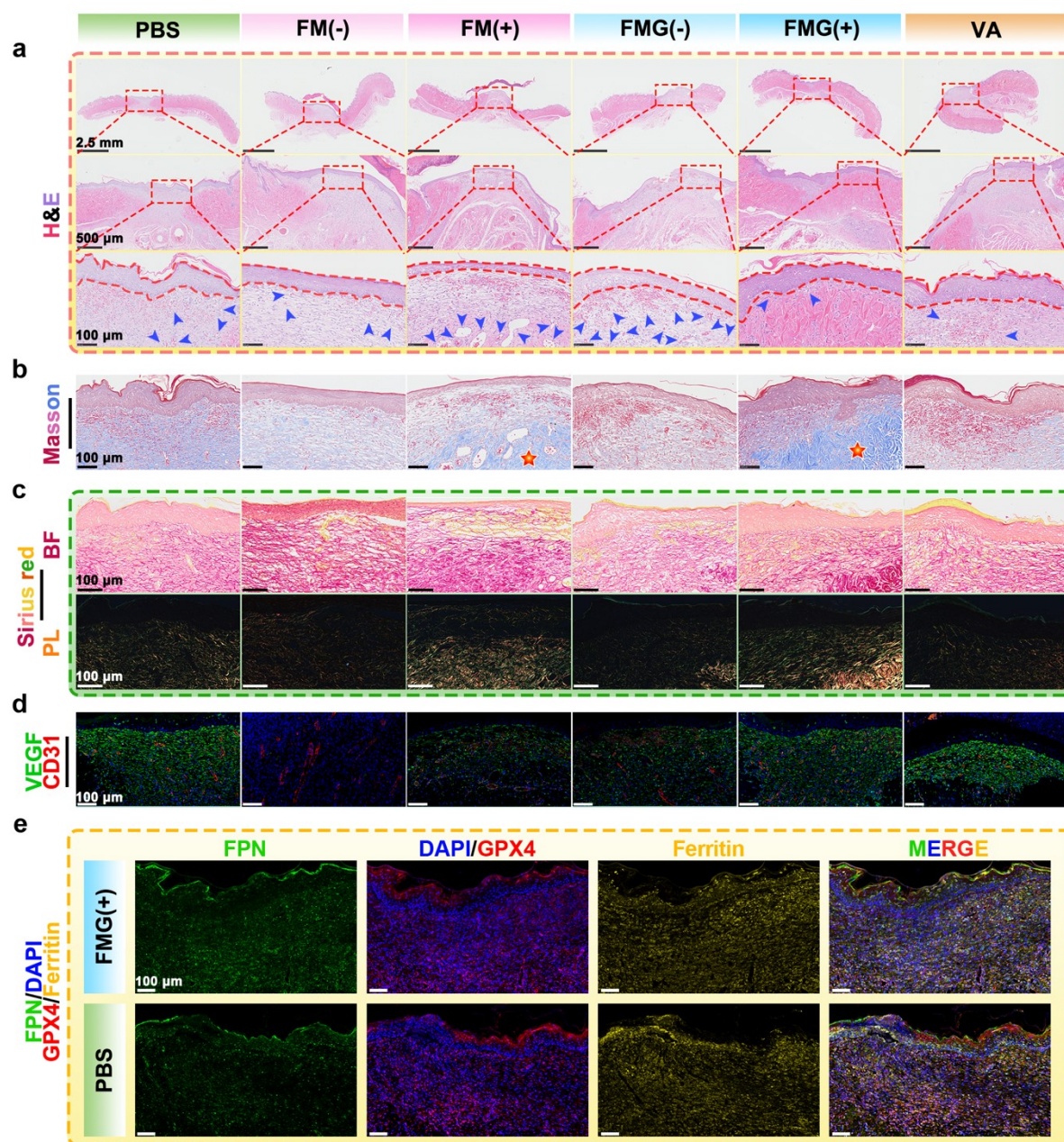


**Figure 10.** Histopathologic images showing wound healing, collagen deposition, angiogenesis, and ferroptosis. (a) H&E staining results of cutaneous tissues (the blue arrow represents the new vessels). (b) Masson's trichrome staining result (the red star indicates the collagen deposition). (c) Sirius red staining result (BF: bright field; PL: polarized light). (d) Immunofluorescence staining of VEGF (green) and CD31 (red) after different treatments. DAPI stained cell nucleus (blue). (e)

Immunofluorescence images of FPN (green), GPX4 (red) and ferritin (yellow) after different treatments. DAPI stained cell nucleus (blue).

### 3. Conclusion

Collectively, we successfully fabricated novel F-bio-HJ to realize short-term efficient extra-intracellular sterilization and tissue regeneration in infected diabetic wounds (**Figure 9g**). With NIR, the F-bio-HJ exhibits outstanding photothermal, photodynamic, and chemodynamic properties. With proper hyperthermal effect and abundant ROS, the bacterial membrane structure of the extracellular bacteria is damaged, allowing ROS and  $\text{Fe}^{2+}$  to accumulate in bacteria. GOx consumes  $\text{O}_2$  to convert glucose into gluconic acid and  $\text{H}_2\text{O}_2$ , creating a “hunger” environment. After consuming GSH, F-bio-HJ can eliminate bacteria *via* ferroptosis with typical characteristics including lipid peroxidation, MDA accumulation, metabolism dysfunction, and genetic processing dysfunction. Simultaneously, F-bio-HJ can deliver  $\text{Fe}^{2+}$  to cells at an early stage to assist macrophages in accumulating ferroptotic pressure to attack the engulfed bacteria and rapidly complete the process of intracellular sterilization. After the sterilization process, the cells deliver antioxidant substances through overexpression of FPN, and the hunger environment activates AMPK to avoid cellular ferroptosis, protect macrophage function, mitigate the inflammatory expression of macrophages, enable rapid conversion from the inflammatory state to the repair state, and promote cutaneous tissue regeneration. Accordingly, this work provides the design of bacteria-targeted bio-HJs to inspire versatile therapeutic strategies or candidate drugs for multiple infectious diseases.

### 4. Experimental Section

#### Ethical Approval

All procedures concerning animals were approved and authorized by the Research Ethics Committee of West China Hospital of Stomatology (No. WCHSIRB-D-2022-280). All surgical procedures followed the standard guidelines.

#### Statistical Analysis

This article is protected by copyright. All rights reserved.

All experiments were performed as biological replicates at least three times. All data were expressed as mean values  $\pm$  standard derivation (SD). All the quantitative data in each experiment were evaluated and analyzed using Student's t-test for two-group analysis or one-way ANOVA and Tukey's multiple comparisons test for multiple-group analysis in GraphPad Prism 9.0 software to evaluate the statistical significance of the variance. The "ns" presents  $p > 0.05$ , and a  $p$ -value of  $<0.05$  was used as a statistical significance threshold.

Other methods and any associated references are available in the Supporting Information.

### Supporting Information

Supporting Information is available from the Wiley Online Library or from the author.

### Acknowledgments

W.D. and R.S. contributed equally to this work. This work is jointly funded by the National Natural Science Foundation of China (32271392, 82071146, 81961160736, 81870804), Natural Science Foundation of Sichuan (2022NSFSC0361, 2023NSFSC0333, 2023NSFSC0569), Sichuan Science and Technology Program (2021YJ0014, 2021YJ0452), National Key Research and Development Plan (2022YFC2405703), China Oral Health Foundation (A2021-122), Align Technology Specialized Scientific Research Fund (21H0922), Chengdu International Science and Technology Cooperation Foundation (2020-GH03-00005-HZ, 2017-GH02-00025-HZ), State Key Laboratory of Polymer Materials Engineering (sklpme2019-2-05), Young Elite Scientist Sponsorship Program by CAST, Sichuan University-Luzhou City Special Funding for Strategic Cooperation (2020CDLZ-5), the Fundamental Research Funds for the Central Universities (SCU), as well as Hong Kong Scholar. The authors thank Hui Wang, Daichuan Ma, and Daibing Luo (Analytical & Testing Center, Sichuan University) for their help in SEM, XRD, and UV-vis characterizations; Wen Tian and Yanping Huang (Center of Engineering Experimental Teaching, School of Chemical Engineering, Sichuan University) for their help with SEM and TEM measurements; Chaoliang Zhang and Bomiao Cui (State Key Laboratory of Oral Disease, West China Hospital of Stomatology, Sichuan University) for assistance with SEM and CLSM; Han Kang in Life Science Core Facilities (College of Life Sciences, Sichuan

This article is protected by copyright. All rights reserved.

University) with Digital scanning system (WISLEAP WS-10 and Olympus VS200). Part of the figures were created with BioRender.com.

### Conflict of Interest

The authors declare no conflict of interests.

### Data availability statement

All data needed to evaluate the conclusions in the paper are present in the paper and/or the Supplementary Information.

Received: ((will be filled in by the editorial staff))

Revised: ((will be filled in by the editorial staff))

Published online: ((will be filled in by the editorial staff))

### References

- [1] K. Ortmayr, R. de la Cruz Moreno, M. Zampieri, *Nat. Chem. Biol.* **2022**, *18*, 584.
- [2] A. R. Brochado, A. Telzerow, J. Bobonis, M. Banzhaf, A. Mateus, J. Selkrig, E. Huth, S. Bassler, J. Zamarreño Beas, M. Zietek, N. Ng, S. Foerster, B. Ezraty, B. Py, F. Barras, M. M. Savitski, P. Bork, S. Göttig, A. Typas, *Nature* **2018**, *559*, 259.
- [3] S. Baker, N. Thomson, F.-X. Weill, K. E. Holt, *Science* **2018**, *360*, 733.
- [4] S. Hussain, J. Joo, J. Kang, B. Kim, G. B. Braun, Z.-G. She, D. Kim, A. P. Mann, T. Mölder, T. Teesalu, S. Carnazza, S. Guglielmino, M. J. Sailor, E. Ruoslahti, *Nat. Biomed. Eng.* **2018**, *2*, 95.
- [5] X. Liu, Y. Wu, C. Mao, J. Shen, K. Zhu, *Trends Microbiol.* **2022**, *30*, 761.

This article is protected by copyright. All rights reserved.

- [6] D. E. Rogers, *J. Exp. Med.* **1956**, *103*, 713.
- [7] D. L. LaRock, A. F. Johnson, S. Wilde, J. S. Sands, M. P. Monteiro, C. N. LaRock, *Nature* **2022**, *605*, 527.
- [8] M. W. Martynowycz, A. Rice, K. Andreev, T. M. Nobre, I. Kuzmenko, J. Wereszczynski, D. Gidalevitz, *ACS Infect. Dis.* **2019**, *5*, 1214.
- [9] C. Garzoni, W. L. Kelley, *EMBO Mol. Med.* **2011**, *3*, 115.
- [10] P. Ma, H. M. Amemiya, L. L. He, S. J. Gandhi, R. Nicol, R. P. Bhattacharyya, C. S. Smillie, D. T. Hung, *Cell* **2023**, *186*, 877.
- [11] J. A. N. Alexander, L. J. Worrall, J. Hu, M. Vuckovic, N. Satishkumar, R. Poon, S. Sobhanifar, F. I. Rosell, J. Jenkins, D. Chiang, W. A. Mosimann, H. F. Chambers, M. Paetzel, S. S. Chatterjee, N. C. J. Strynadka, *Nature* **2023**, *613*, 375.
- [12] A. R. Zelmer, R. Nelson, K. Richter, G. J. Atkins, *Bone Res.* **2022**, *10*, 1.
- [13] S. Ghosh, M. Sinha, R. Samanta, S. Sadhasivam, A. Bhattacharyya, A. Nandy, S. Saini, N. Tandon, H. Singh, S. Gupta, A. Chauhan, K. K. Aavula, S. S. Varghese, P. Shi, S. Ghosh, M. K. Garg, T. Saha, A. Padhye, S. Ghosh, H. L. Jang, S. Sengupta, *Nat. Biomed. Eng.* **2022**, *6*, 1180.
- [14] J. Li, Z. Li, X. Liu, C. Li, Y. Zheng, K. W. K. Yeung, Z. Cui, Y. Liang, S. Zhu, W. Hu, Y. Qi, T. Zhang, X. Wang, S. Wu, *Nat. Commun.* **2021**, *12*, 1224.
- [15] R. Ma, L. Fang, L. Chen, X. Wang, J. Jiang, L. Gao, *Theranostics* **2022**, *12*, 2266.
- [16] X. Shen, R. Ma, Y. Huang, L. Chen, Z. Xu, D. Li, X. Meng, K. Fan, J. Xi, X. Yan, H. Koo, Y. Yang, J. Jiang, L. Gao, *Nano Today* **2020**, *35*, 100981.
- [17] M. Conrad, V. E. Kagan, H. Bayir, G. C. Pagnussat, B. Head, M. G. Traber, B. R. Stockwell, *Genes Dev.* **2018**, *32*, 602.
- [18] X. Jiang, B. R. Stockwell, M. Conrad, *Nat. Rev. Mol. Cell Biol.* **2021**, *22*, 266.
- [19] Y. Xue, L. Zhang, F. Liu, F. Dai, L. Kong, D. Ma, Y. Han, *ACS Nano* **2023**, *17*, 2711.

- [20] W. Zhu, J. Mei, X. Zhang, J. Zhou, D. Xu, Z. Su, S. Fang, J. Wang, X. Zhang, C. Zhu, *Adv. Mater.* **2022**, *34*, 2207961.
- [21] B. Sun, X. Wang, Z. Ye, J. Zhang, X. Chen, N. Zhou, M. Zhang, C. Yao, F. Wu, J. Shen, *Adv. Sci.* **2023**, *10*, 2207507.
- [22] H. Hu, S. Y. Hua, X. Lin, F. Lu, W. Zhang, L. Zhou, J. Cui, R. Wang, J. Xia, F. Xu, X. Chen, M. Zhou, *ACS Nano* **2023**, *17*, 11692.
- [23] W. Bao, P. Pang, X. Zhou, F. Hu, W. Xiong, K. Chen, J. Wang, F. Wang, D. Xie, Y. Hu, Z. Han, H. Zhang, W. Wang, P. T. Nelson, J. Chen, Y. Lu, H. Man, D. Liu, L. Zhu, *Cell Death Differ.* **2021**, *28*, 1548.
- [24] B. R. Stockwell, J. P. F. Angeli, H. Bayir, A. I. Bush, M. Conrad, S. J. Dixon, S. Fulda, S. Gascón, S. K. Hatzios, V. E. Kagan, K. Noel, X. Jiang, A. Linkermann, M. E. Murphy, M. Overholtzer, A. Oyagi, G. C. Pagnussat, J. Park, Q. Ran, C. S. Rosenfeld, K. Salnikow, D. Tang, F. M. Torti, S. V. Torti, S. Toyokuni, K. A. Woerpel, D. D. Zhang, *Cell* **2017**, *171*, 273.
- [25] K. Bersuker, J. M. Hendricks, Z. Li, L. Magtanong, B. Ford, P. H. Tang, M. A. Roberts, B. Tong, T. J. Maimone, R. Zoncu, M. C. Bassik, D. K. Nomura, S. J. Dixon, J. A. Olzmann, *Nature* **2019**, *575*, 688.
- [26] M. Gao, P. Monian, N. Quadri, R. Ramasamy, X. Jiang, *Mol. Cell* **2015**, *59*, 298.
- [27] M. Luo, L. Wu, K. Zhang, H. Wang, T. Zhang, L. Gutierrez, D. O'Connell, P. Zhang, Y. Li, T. Gao, W. Ren, Y. Yang, *Cell Death Differ.* **2018**, *25*, 1457.
- [28] W. S. Yang, R. SriRamaratnam, M. E. Welsch, K. Shimada, R. Skouta, V. S. Viswanathan, J. H. Cheah, P. A. Clemons, A. F. Shamji, C. B. Clish, L. M. Brown, A. W. Girotti, V. W. Cornish, S. L. Schreiber, B. R. Stockwell, *Cell* **2014**, *156*, 317.
- [29] S. Doll, F. P. Freitas, R. Shah, M. Aldrovandi, M. C. da Silva, I. Ingold, A. Goya Grocin, T. N. Xavier da Silva, E. Panzilius, C. H. Scheel, A. Mourão, K. Buday, M. Sato, J. Wanninger, T. Vignane, V. Mohana, M. Rehberg, A. Flatley, A. Schepers, A. Kurz, D. White, M. Sauer, M. Sattler, E. W. Tate, W. Schmitz, A. Schulze, V. O'Donnell, B. Proneth, G. M. Popowicz, D. A. Pratt, J. P. F. Angeli, M. Conrad, *Nature* **2019**, *575*, 693.

This article is protected by copyright. All rights reserved.

- [30] V. A. N. Kraft, C. T. Bezjian, S. Pfeiffer, L. Ringelstetter, C. Müller, F. Zandkarimi, J. Merl-Pham, X. Bao, N. Anastasov, J. Kössl, S. Brandner, J. D. Daniels, P. Schmitt-Kopplin, S. M. Hauck, B. R. Stockwell, K. Hadian, J. A. Schick, *ACS Cent. Sci.* **2020**, *6*, 41.
- [31] C. Mao, X. Liu, Y. Zhang, G. Lei, Y. Yan, H. Lee, P. Koppula, S. Wu, L. Zhuang, B. Fang, M. V. Poyurovsky, K. Olszewski, B. Gan, *Nature* **2021**, *593*, 586.
- [32] W. S. Yang, K. J. Kim, M. M. Gaschler, M. Patel, M. S. Shchepinov, B. R. Stockwell, *Proc. Natl. Acad. Sci. U. S. A.* **2016**, *113*, 4966.
- [33] H. Lee, F. Zandkarimi, Y. Zhang, J. K. Meena, J. Kim, L. Zhuang, S. Tyagi, L. Ma, T. F. Westbrook, G. R. Steinberg, D. Nakada, B. R. Stockwell, B. Gan, *Nat. Cell Biol.* **2020**, *22*, 225.
- [34] C. Pan, Z. Mao, X. Yuan, H. Zhang, L. Mei, X. Ji, *Adv. Sci.* **2022**, *9*, 2105747.
- [35] B. Li, R. Shu, W. Dai, F. Yang, H. Xu, X. Shi, Y. Li, D. Bai, W. Yang, Y. Deng, *Small* **2022**, *18*, 2203619.
- [36] Z. Wang, B. Du, X. Gao, Y. Huang, M. Li, Z. Yu, J. Li, X. Shi, Y. Deng, K. Liang, *Nano Today* **2022**, *46*, 101595.
- [37] A. Y. Satoh, J. E. Trosko, S. J. Masten, *Environ. Sci. Technol.* **2007**, *41*, 2881.
- [38] X. Li, C. Kong, Z. Chen, *ACS Appl. Mater. Interfaces* **2019**, *11*, 9504.
- [39] H. J. Forman, H. Zhang, *Nat. Rev. Drug Discov.* **2021**, *20*, 689.
- [40] H. J. Forman, H. Zhang, A. Rinna, *Mol. Aspects Med.* **2009**, *30*, 1.
- [41] M. Zhao, X. Xie, C. E. Ren, T. Makaryan, B. Anasori, G. Wang, Y. Gogotsi, *Adv. Mater.* **2017**, *29*, 1702410.
- [42] Z. Yang, X. Fu, D. Ma, Y. Wang, L. Peng, J. Shi, J. Sun, X. Gan, Y. Deng, W. Yang, *Small* **2021**, *17*, 2103993.
- [43] Y. Yang, X. Zhou, Y. K. Chan, Z. Wang, L. Li, J. Li, K. Liang, Y. Deng, *Small* **2022**, *18*, 2105988.

- [44] L. Wang, S. Xie, Z. Wang, F. Liu, Y. Yang, C. Tang, X. Wu, P. Liu, Y. Li, H. Saiyin, S. Zheng, X. Sun, F. Xu, H. Yu, H. Peng, *Nat Biomed Eng* **2020**, *4*, 159.
- [45] Y. Yu, L. Jiang, H. Wang, Z. Shen, Q. Cheng, P. Zhang, J. Wang, Q. Wu, X. Fang, L. Duan, S. Wang, K. Wang, P. An, T. Shao, R. T. Chung, S. Zheng, J. Min, F. Wang, *Blood* **2020**, *136*, 726.
- [46] M. Gao, P. Monian, Q. Pan, W. Zhang, J. Xiang, X. Jiang, *Cell Res* **2016**, *26*, 1021.
- [47] B. L. Furman, *Current Protocols* **2021**, *1*, 78.

### Table of Contents

A precise ferroptosis bio-heterojunction (F-bio-HJ) consisting of  $\text{Fe}_2\text{O}_3$ ,  $\text{Ti}_3\text{C}_2$ -MXene, and glucose oxidase is developed to induce extra-intracellular bacteria-targeted ferroptosis for infected diabetic cutaneous regeneration. Under NIR irradiation, F-bio-HJ induces extracellular bacterial ferroptosis *via* photothermal, photodynamic and chemodynamic properties and assists macrophages against intracellular bacteria *via* ferroportin-mediated bacterial ferroptosis and hunger-triggered AMPK pathway-mediated cell protection, elevating the biocompatibility of ferroptosis-mediated therapeutic strategies.

